A SEARCH FOR LONG-LIVED, CHARGED, SUPERSYMMETRIC PARTICLES USING IONIZATION WITH THE ATLAS DETECTOR

BRADLEY AXEN

September 2016 – Version 0.31

Usually a quotation.

Dedicated to.

ABSTRACT

How to write a good abstract:

https://plg.uwaterloo.ca/~migod/research/beck00PSLA.html

PUBLICATIONS

Some ideas and figures have appeared previously in the following publications:

Put your publications from the thesis here. The packages `multibib` or `bibtopic` etc. can be used to handle multiple different bibliographies in your document.

ACKNOWLEDGEMENTS

Put your acknowledgements here.

And potentially a second round.

CONTENTS

LIST OF FIGURES

LIST OF TABLES

LISTINGS

ACRONYMS

SM Standard Model

LSP Lightest Supersymmetric Particle

LHC Large Hadron Collider

ToT time over threshold

LCW local cluster weighted

MIP minimally ionizing particle

EPJC European Physical Journal C

JES jet energy scale

LLP Long-Lived Particle

CR Control Region

PART I

INTRODUCTION

You can put some informational part preamble text here.

1 INTRODUCTION

PART II

THEORETICAL CONTEXT

You can put some informational part preamble text here.

2 STANDARD MODEL

The SM of particle physics seeks to explain the symmetries and interactions of all currently discovered fundamental particles. It has been tested by several generations of experiments and has been remarkably succesful, no significant deviations have been found. The SM provides predictions in particle physics for interactions up to the Planck scale (10^{15}-10^{19} GeV).

The theory itself is a quantum field theory grown from an underlying $SU(3) \times SU(2) \times U(1)$ that requires the particle content and quantum numbers consistent with experimental observations (see Section 2.1). Each postulated symmetry is accompanied by an interaction between particles through gauge invariance. These interactions are referred to as the Strong, Weak, and Electromagnetic forces, which are discussed in Section 2.2.

Although this model has been very predictive, the theory is incomplete; for example, it is not able to describe gravity or astronomically observed dark matter. These limitations are discussed in more detail in Section 2.3.

2.1 PARTICLES

The most familiar matter in the universe is made up of protons, neutrons, and electrons. Protons and neutrons are composite particles, however, and are made up in turn by particles called quarks. Quarks carry both electric charge and color charge, and are bound in color-neutral combinations called baryons. The electron is an example of a lepton, and carries only electric charge. Another type of particle, the neutrino, does not form atomic structures in the same way that quarks and leptons do because it carries no color or electric charge. Collectively, these types of particles are known as fermions, the group of particles with half-integer spin.

There are three generations of fermions, although familiar matter is formed predominantly by the first generation. The generations are identical except for their masses, which increase in each generation by convention. In addition, each of these particles is accompanied by an antiparticle, with opposite-sign quantum numbers but the same mass.

The fermions compromise what is typically considered matter, but there are additional particles that are mediators of interactions between those fermions. These mediators are known as the gauge bosons, gauge in that their existance is required by gauge invariance (discussed further in Section 2.2) and bosons in that they have integer spin. The boson which mediates the electromagnetic force is the photon, the first boson to be discovered; it has no electric charge, no mass, and a spin of 1. There are three spin-1 mediators of the weak force, the two W bosons and the Z boson. The W bosons have electric charge of $\pm$ 1 and a mass of 80.385 ± 0.015 GeV, while the Z boson is neutral and has a mass of

91.1876 ± 0.0021 GeV. The strong force is mediated by eight particles called gluons, which are massless and electrically neutral but do carry color charge.

The final particle present in the SM is the Higgs boson, which was recently observed for the first time by experiments at CERN in 2012. It is electrically neutral, has a mass of 125.7 ± 0.4 Gev, and is the only spin-0 particle yet to be observed. The Higgs boson is the gauge boson associated with the mechanism that gives a mass to the W and Z bosons.

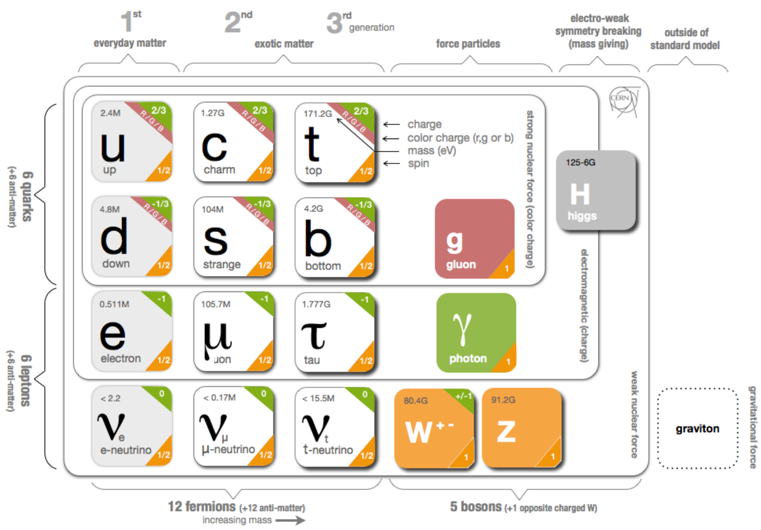

Figure 1: The particle content of the SM.

Together these particles form the entire content of the SM, and are summarized in Figure 1. These are the particles that constitute the observable universe and all the so-far-observed interactions within it.

2.2 INTERACTIONS

The interactions predicted and described by the SM are fundamentally tied to the particles within it, both in that they describe the way those particles can influence each other and also in that the existence of the interactions requires the existence of some particles (the gauge bosons).

2.3 LIMITATIONS

3 SUPERSYMMETRY

3.1 MOTIVATION

3.2 STRUCTURE

3.3 PHENOMENOLOGY

4 LONG-LIVED PARTICLES

4.1 MECHANISMS

4.1.1 EXAMPLES IN SUPERSYMMETRY

4.2 PHENOMENOLOGY

4.2.1 DISIMILARITIES TO PROMPT DECAYS

4.2.2 CHARACTERISTIC SIGNATURES

PART III

EXPERIMENTAL STRUCTURE AND RECONSTRUCTION

You can put some informational part preamble text here.

5 THE LARGE HADRON COLLIDER

5.1 INJECTION CHAIN

5.2 DESIGN AND PARAMETERS

5.3 LUMINOSITY

6 THE ATLAS DETECTOR

6.1 COORDINATE SYSTEM

6.2 MAGNETIC FIELD

6.3 INNER DETECTOR

6.3.1 PIXEL DETECTOR

6.3.2 SEMICONDUCTOR TRACKER

6.3.3 TRANSITION RADIATION TRACKER

6.4 CALORIMETRY

6.4.1 ELECTROMAGNETIC CALORIMETERS

6.4.2 HADRONIC CALORIMETERS

6.4.3 FORWARD CALORIMETERS

6.5 MUON SPECTROMETER

6.6 TRIGGER

6.6.1 TRIGGER SCHEME

6.6.2 MISSING TRANSVERSE ENERGY TRIGGERS

7 EVENT RECONSTRUCTION

The ATLAS experiment combines measurements in the subdetectors to form a cohesive picture of each physics event.

7.1 TRACKS AND VERTICES

7.1.1 TRACK RECONSTRUCTION

7.1.1.1 NEURAL NETWORK

7.1.1.2 PIXEL DE/DX

7.1.2 VERTEX RECONSTRUCTION

7.2 JETS

7.2.1 TOPOLOGICAL CLUSTERING

7.2.2 JET ENERGY SCALE

7.2.3 JET ENERGY SCALE UNCERTAINTIES

7.2.4 JET ENERGY RESOLUTION

7.3 ELECTRONS

7.3.1 ELECTRON IDENTIFICATION

7.4 MUONS

7.4.1 MUON IDENTIFICATION

7.5 MISSING TRANSVERSE ENERGY

PART IV

CALORIMETER RESPONSE

You can put some informational part preamble text here.

8 RESPONSE MEASUREMENT WITH SINGLE HADRONS

As discussed in Section 7.2, colored particles produced in collisions hadronize into jets of multiple hadrons. One approach to understanding jet energy measurements in the ATLAS calorimeters is to evaluate the calorimeter response to those individual hadrons; measurements of individual hadrons can be used to build up an understanding of the jets that they form. The redundancy of the momentum provided by the tracking system and the energy provided by the calorimeter provides an opportunity to study calorimeter response using real collisions, as described further in Section 8.2.

Calorimeter response includes a number of physical effects that can be extracted to provide insight into many aspects of jet modeling. First, many charged hadrons interact with the material of the detector prior to reaching the calorimeters and thus do not deposit any energy. Comparing this effect in data and simulation is a powerful tool in validating the interactions of particles with the material of the detector and the model of the detector geometry in simulation, see Section 8.2.2. The particles which do reach the calorimeter deposit their energy into several adjacent cells, which are then clustered together. The energy of the cluster is then the total energy deposited by that particle. Comparing the response of hadrons in data to that of simulated hadrons provides a direct evaluation of the showering of hadronic particles and the energy deposited by particles in matter (Section 8.2.4).

The above studies all use an inclusive selection of charged particles, which are comprised predominantly of pions, kaons, and (anti)protons. It is also possible to measure the response to various identified particle types separately to evaluate the simulated interactions of each particle, particularly at low energies where differences between species are very relevant. Pions and (anti)protons can be identified through decays of long-lived particles, in particular Λ, $\overline{\Lambda}$, and K^0_S, and then used to measure response as described above. This is discussed in detail in Section 8.3.

Together, these measurements in data provide a thorough understanding of the way hadrons interact with the ATLAS detector and can be used to build up a description of jets, as seen in Chapter 9. The results in this chapter use data collected at 7 and 8 TeV collected in 2010 and 2012, respectively. Both are included as the calorimeter was repaired and recalibrated between those two data-taking periods. Both sets of data are compared to an updated simulation that includes new physics models provided by `Geant4` [1] and improvements in the detector description [2, 3]. These results are published in European Physical Journal C (EPJC) [4] and can be compared to a similar measurement performed in 2009 and 2010 [5], which used the previous version of the simulation framework [6].

8.1 DATASET AND SIMULATION

8.1.1 DATA SAMPLES

The two datasets used in this chapter are taken from dedicated low-pileup runs where the fraction of events with multiple interactions was negligible, to facilitate measurement of isolated hadrons. The 2012 dataset at $\sqrt{s} = 8$ TeV contains 8 million events and corresponds to an integrated luminosity of 0.1 nb^{-1}. The 2010 dataset at $\sqrt{s} = 7$ TeV contains 3 million events and corresponds to an integrated luminosity of 3.2 nb^{-1}. The latter dataset was also used in the 2010 results [5], but it has since been reanalyzed with an updated detector description for the material and alignment.

8.1.2 SIMULATED SAMPLES

The two datasets above are compared to simulated single-, double-, and non-diffractive events generated with `Pythia8` [7] using the A2 configuration of hadronization [8] and the MSTW 2008 parton-distribution function set [9, 10]. The conditions and energies for each run are matched in the two simulations.

To evaluate the interaction of hadrons with detector material, the simulation uses two different collections of hadronic physics models, called physics lists, in `Geant4 9.4` [11]. The first, `QGSP_BERT`, combines the Bertini intra-nuclear cascade [12–14] below 9.9 GeV, a parametrized proton inelastic model from 9.5 to 25 GeV [15], and a quark-gluon string model above 12 GeV [16–20]. The second, `FTFP_BERT`, combines the Bertini intra-nuclear cascade [12–14] below 5 GeV and the Fritiof model [21–24] above 4 GeV. In either list, `Geant4` enforces a smooth transition between models where multiple models overlap.

8.1.3 EVENT SELECTION

The event selection for this study is minimal, as the only requirement is selecting good-quality events with an isolated track. Such events are triggered by requiring at least two hits in the minimum-bias trigger scintillators. After trigger, each event is required to have exactly one reconstructed vertex, and that vertex is required to have four or more associated tracks.

The particles which enter into the response measurements are first identified as tracks in the inner detector. The tracks are required to have at least 500 MeV of transverse momentum. To ensure a reliable momentum measurement, these tracks are required to have at least one hit in the pixel detector, six hits in the SCT, and small longitudinal and transverse impact parameters with respect to the primary vertex [5]. For the majority of the measurements in this chapter, the track is additionally required to have 20 hits in the TRT, which significantly reduces the contribution from tracks which undergo nuclear interactions. This requirement and its effect is discussed in more detail in Section 8.2.4.1. In addition, tracks are rejected if there is another track which extrapolates to the calorimeter within a cone of $\Delta R = \sqrt{(\Delta\phi)^2 + (\Delta\eta)^2} < 0.4$. This requirement guarantees that the contamination of energy from nearby charged particles is negligible [5].

8.2 INCLUSIVE HADRON RESPONSE

The calorimeter response is more precisely defined as the ratio of the measured calorimeter energy to the true energy carried by the particle, although this true energy is unknown. For charged particles, however, the inner detector provides a very precise measurement of momentum (with uncertainty less than 1%) that can be used as a proxy for true energy. The ratio of the energy deposited by the charged particle in the calorimeter, E, to its momentum measured in the inner detector p, forms the calorimeter response measure called E/p. Though the distribution of E/p contains a number of physical features, this study focuses on the trends in two aggregated quantities: $\langle E/p \rangle$, the average of E/p within a given subset of particles, and the zero fraction, the fraction of particles with no associated energy in the calorimeter.

The calorimeter energy assigned to a track particle is defined using clusters. The clusters are formed using a 4–2–0 algorithm [25] that begins with seeds requiring at least 4 times the average calorimeter noise. The neighboring cells with at least twice that noise threshold are then added to the cluster, and all bounding cells are then added with no requirement. This algorithm minimizes noise contributions through its seeding process, and including the additional layers improves the energy resolution [26]. The clusters are associated to a given track if they fall within a cone of $\Delta R = 0.2$ of the extrapolated position of the track, which includes about 90% of the energy on average [5]. This construction is illustrated in Figure 2.

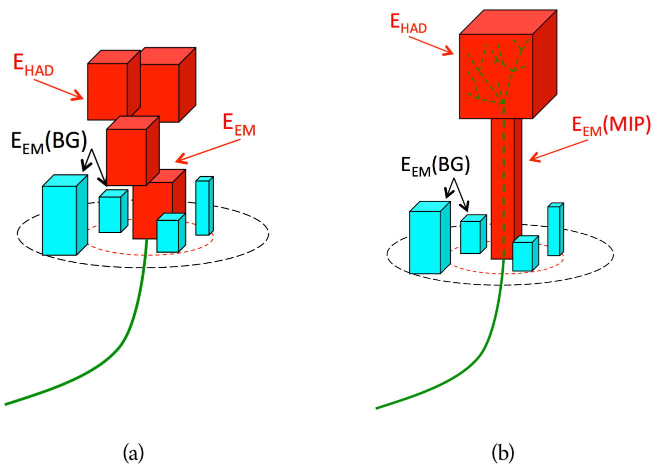

Figure 2: An illustration (a) of the E/p variable used throughout this paper. The red energy deposits come from the charged particle targeted for measurement, while the blue energy deposits are from nearby neutral particles and must be subtracted. The same diagram (b) for the neutral-background selection, described in Section 8.2.3.

8.2.1 E/P DISTRIBUTION

The E/p distributions measured in both data and simulation are shown in Figure 3 for two example bins of track momentum and for tracks in the central region of the detector. These distributions show several important features of the E/p observable. The large content in the bin at $E = 0$ comes from tracks that have no associated cluster, which occurs due to interactions with detector material prior to reaching the calorimeter or the energy deposit being insufficiently large to generate a seed, and are discussed in Section 8.2.2. The small negative tail comes from similar tracks that do not deposit any energy in the calorimeter but are randomly associated to a noise cluster. The long positive tail above 1.0 comes from the contribution of neutral particles. Nearby neutral particles deposit (sometimes large) additional energy in the calorimeter but do not produce tracks in the inner detector, so they cannot be rejected by the track isolation requirement. Additionally the peak and mean of the distribution falls below 1.0 because of the loss of energy not found within the cone as well as the non-compensation of the calorimeter.

The data and simulation share the same features, but the high and low tails are significantly different. The simulated events tend to overestimate the contribution of neutral particles to the long tail, an effect which can be isolated and removed as discussed in Section 8.2.3. Additionally, the simulated clusters have less noise on average, although this is a small effect on the overall response.

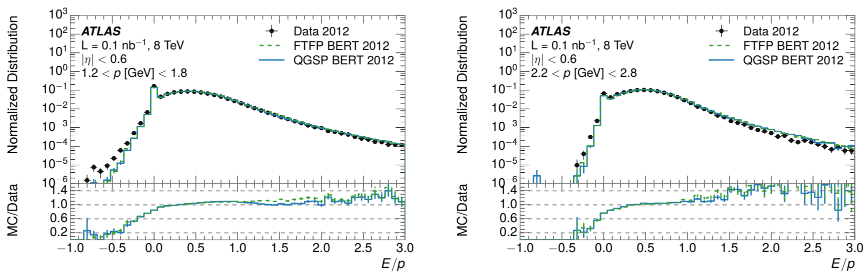

(a) (b)

Figure 3: The E/p distribution and ratio of simulation to data for isolated tracks with (a) $|\eta| < 0.6$ and $1.2 < p/\text{GeV} < 1.8$ and (b) $|\eta| < 0.6$ and $2.2 < p/\text{GeV} < 2.8$.

8.2.2 ZERO FRACTION

The fraction of particles with no associated clusters, or similarly those with $E \leq 0$, reflects the modeling of both the detector geometry and hadronic interactions. The zero fraction is expected to rise as the amount of material a particle traverses increases, while it is expected to decrease as the particle energy increases. This dependence can be seen in Figure 4, where the zero fraction in data and simulation is shown as a function of momentum and the amount of material measured in interaction lengths. The trends are similar between the 2010 and 2012 measurements. The zero fraction decreases with energy as expected. The amount of material in the detector increases with η, which provides a distribution of interaction lengths. As the data and simulation have significant disagreement in the zero fraction over a number of interaction lengths, the difference must be primarily from the modeling of hadronic interactions with detector material and not just the detector geometry.

There is also a noticeable difference between positive and negative tracks at low momentum, which reflects the difference in response between protons and antiprotons. Antiprotons have significant model differences in the two physics lists, `QGSP_BERT` and `FTFP_BERT`, and this is evident in the lowest momentum bin of the data to simulation ratio. This difference is explored further in Section 8.3.

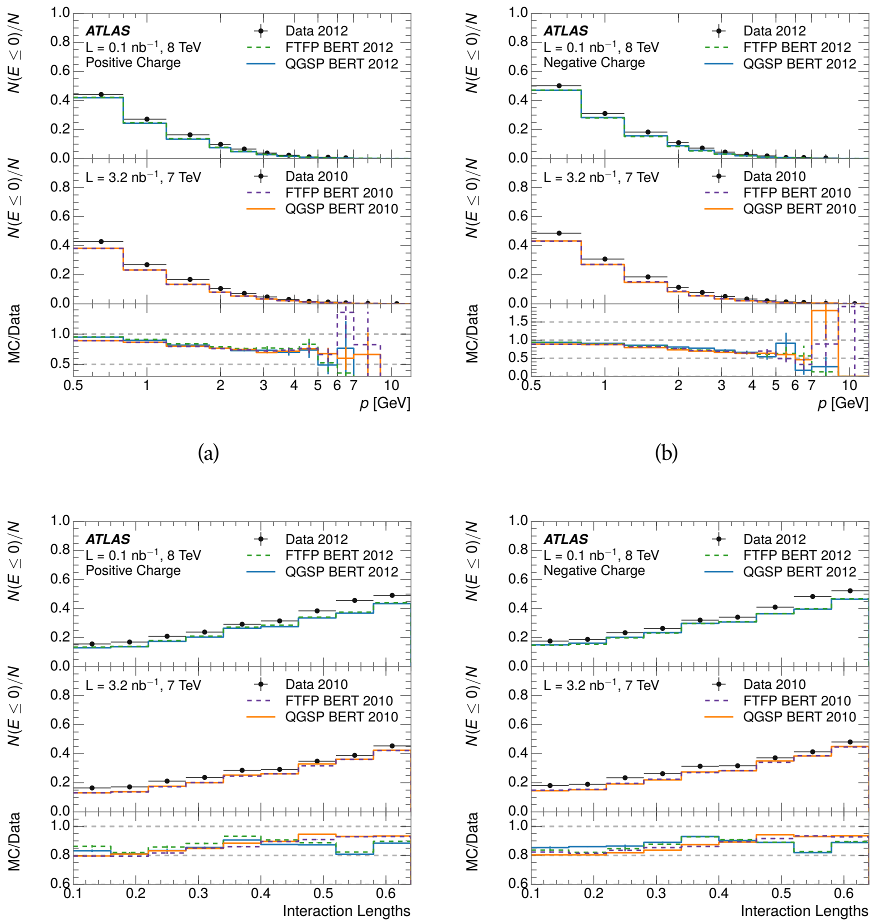

(a) (b) (c) (d)

Figure 4: The fraction of tracks as a function (a, b) of momentum, (c, d) of interaction lengths with $E \leq 0$ for tracks with positive (on the left) and negative (on the right) charge.

8.2.3 NEUTRAL BACKGROUND SUBTRACTION

The isolation requirement on hadrons is only effective in remove energy contribution from nearby charged particles. Nearby neutral particles, predominantly photons from π^0 decays, also add their energy to the calorimeter clusters, but mostly in the electromagnetic calorimeter. It is possible to measure this contribution, on average, using late-showering hadrons that minimally ionize in the electromagnetic calorimeter. Such particles are selected by requiring that they deposit less than 1.1 GeV in the EM calorimeter within a cone of $\Delta R < 0.1$ around the track. To ensure that these particles are well measured, they are additionally required to deposit between 40% and 90% of their energy in the hadronic calorimeter within the same cone.

These particles provide a clean sample to measure the nearby neutral background because they do not deposit energy in the area immediately surrounding them in the EM calorimeter, as shown in Figure 2. So, the energy deposits in the region $0.1 < \Delta R < 0.2$ can be attributed to neutral particles alone. To estimate the contribution to the whole cone considered for the response measurement, that energy is scaled by a geometric factor of 4/3. This quantity, $\langle E/p \rangle_{\mathrm{BG}}$, measured in aggregate over a number of particles, gives the contribution to $\langle E/p \rangle$ from neutral particles in the EM calorimeter. Similar techniques were used in the individual layers of the hadronic calorimeters to show that the background from neutrals is negligible in those layers [5].

The distribution of this background estimate is shown in Figure 5. Although the simulation captures the overall trend, it significantly overestimates the neutral contribution for tracks with momentum between 2 and 8 GeV. This effect was also seen in the tails of the E/p distributions in Figure 3. This difference is likely due to the modeling of coherent neutral particle radiation in `Pythia8`, as the discrepancy does not depend on η and thus is unlikely to be a mismodeling of the detector. This difference can be subtracted to form a corrected average E/p, as in Section 8.2.4.

8.2.4 CORRECTED RESPONSE

Figure 6 shows $\langle E/p \rangle_{\mathrm{COR}}$ as a function of momentum for several bins of pseudorapidity. This corrected $\langle E/p \rangle_{\mathrm{COR}} \equiv \langle E/p \rangle - \langle E/p \rangle_{\mathrm{BG}}$ measures the average calorimeter response without the contamination of neutral particles. It is the most direct measurement of calorimeter response in that it is the energy measured for fully isolated hadrons. The correction is performed separately in data and simulation, so that the mismodeling of the neutral background in simulation is removed from the comparison of response. The simulation overestimates the response at low momentum by about 5%, an effect that can be mostly attributed to the underestimation of the zero fraction mentioned previously.

The response measurement above used topological clustering at the EM scale, that is clusters were formed to measure energy but no corrections were applied to correct for expected effects like energy lost outside of the cluster or in uninstrumented material. It is also interesting to measure $\langle E/p \rangle_{\mathrm{COR}}$ using local clus-

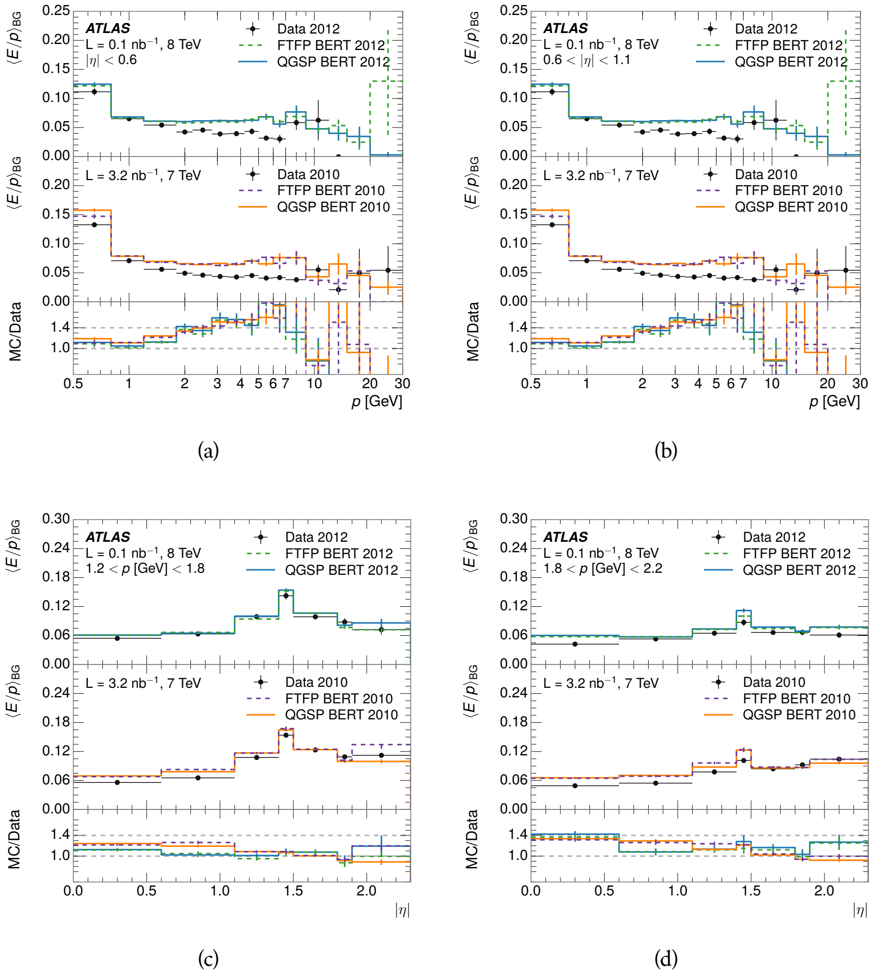

Figure 5: $\langle E/p \rangle_{\mathrm{BG}}$ as a function of the track momentum for tracks with (a) $|\eta| < 0.6$, (b) $0.6 < |\eta| < 1.1$, and as a function of the track pseudorapidity for tracks with (c) $1.2 < p/\mathrm{GeV} < 1.8$, (d) $1.8 < p/\mathrm{GeV} < 2.2$.

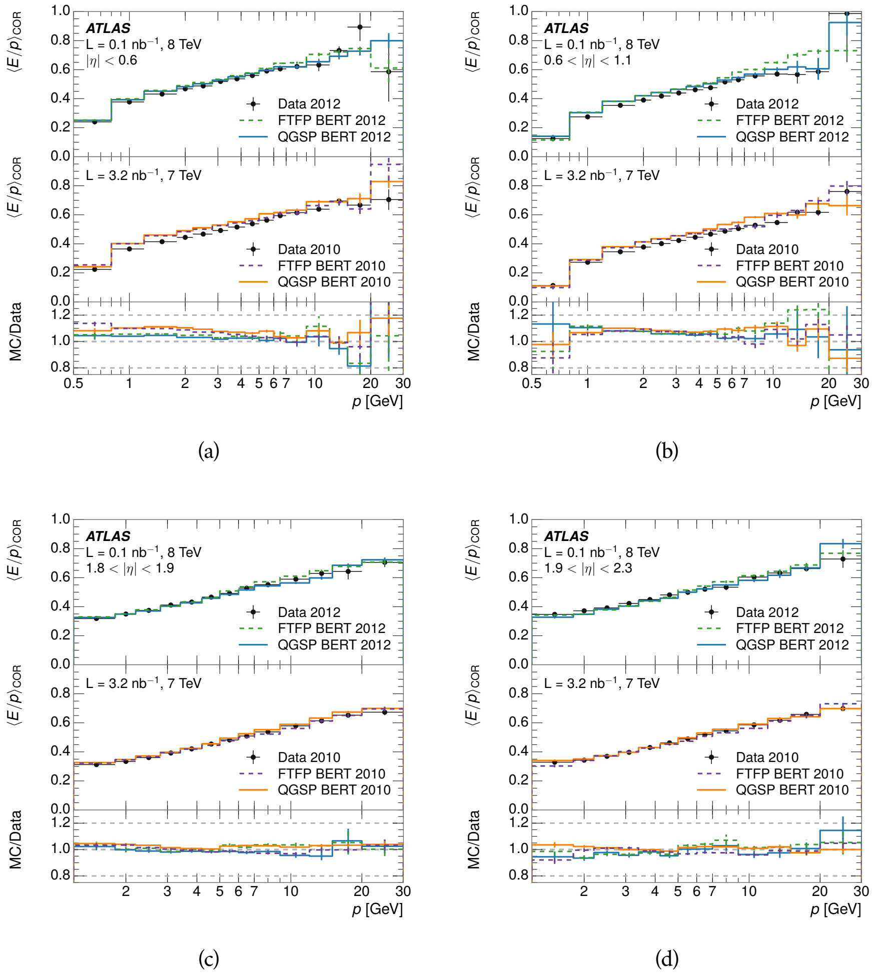

Figure 6: $\langle E/p \rangle_{\text{COR}}$ as a function of track momentum, for tracks with (a) $|\eta| < 0.6$, (b) $0.6 < |\eta| < 1.1$, (c) $1.8 < |\eta| < 1.9$, and (d) $1.9 < |\eta| < 2.3$.

ter weighted (LCW) energies, which accounts for those effects by calibrating the energy based on the properties of the cluster such as energy density and depth in the calorimeter. Figure 7 shows these distributions for tracks with zero or more clusters and separately for tracks with one or more clusters. The calibration moves $\langle E/p \rangle_{\mathrm{COR}}$ significantly closer to 1.0, which is the purpose of the calibration. The agreement between data and simulation improves noticeably when at least one cluster is required, as this removes the contribution from the mismodeling of the zero fraction.

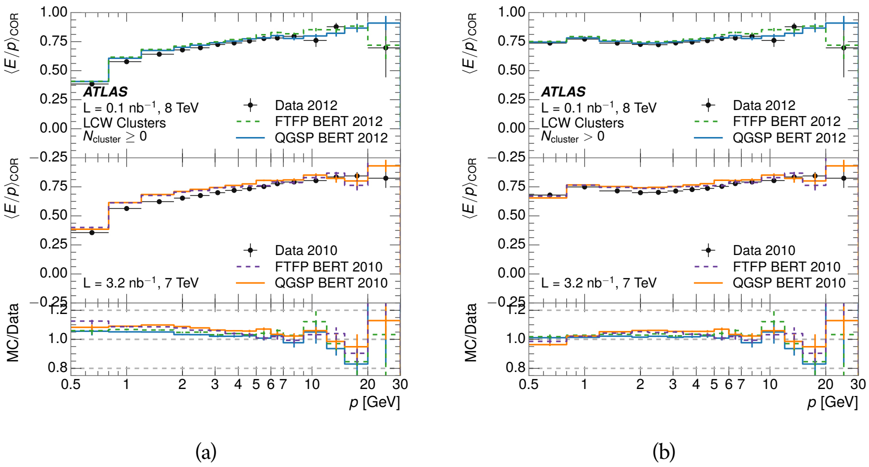

Figure 7: $\langle E/p \rangle_{\mathrm{COR}}$ calculated using LCW-calibrated topological clusters as a function of track momentum for tracks with (a) zero or more associated topological clusters or (b) one or more associated topological clusters.

8.2.4.1 ADDITIONAL STUDIES

As has been seen in several previous measurements, the simulation does not correctly model the chance of a low momentum hadron to reach the calorimeter. Because of the consistent discrepancy across pseudorapidity and interaction lengths, this seems to be best explained by incomplete understanding of hadronic interactions with the detector. For example, a hadron that scatters off of a nucleus in the inner detector can be deflected through a significant angle and not reach the expected location in the calorimeter. In addition, these interactions can produce secondary particles that are difficult to model.

The requirement on the number of hits in the TRT reduces these effects by preferentially selecting tracks that do not undergo nuclear interactions. It is interesting to check how well the simulation models tracks with low numbers of TRT hits, where the nuclear interactions are much more likely. Figure 8 compares the distributions with $N_{\mathrm{TRT}} < 20$ to $N_{\mathrm{TRT}} > 20$ for real and simulated particles. As expected, the tracks with fewer hits are poorly modeled in the simulation as $\langle E/p \rangle_{\mathrm{COR}}$ differs by as much as 25% at low momentum.

Another interesting aspect of the simulation is the description of antiprotons at low momentum, where `QGSP_BERT` and `FTFP_BERT` have significant differences. This can be seen to have an effect in the inclusive response measurement

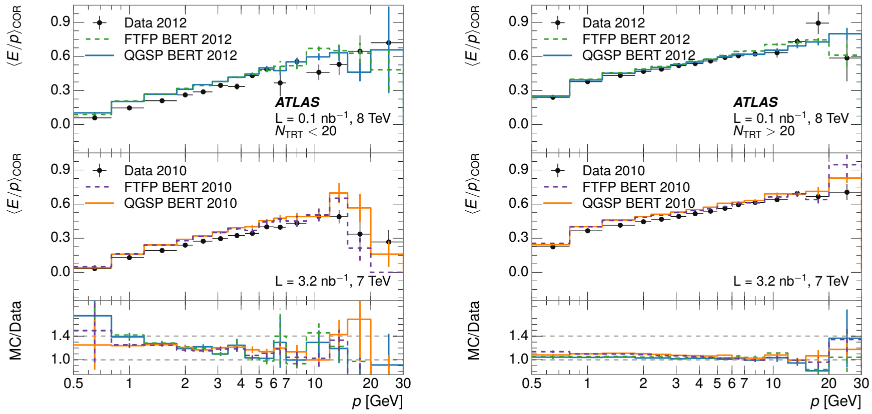

(a) (b)

Figure 8: Comparison of the $\langle E/p \rangle_{\mathrm{COR}}$ for tracks with (a) less than and (b) greater than 20 hits in the TRT.

when separated into positive and negative charge. The $\langle E/p \rangle_{\mathrm{COR}}$ distributions for positive and negative particles are shown in Figure 9, where a small difference between QGSP_BERT and FTFP_BERT can be seen in the distribution for negative tracks. This is demonstrated more clearly in Figure 10, which shows the E/p distribution in the two simulations separated by charge. There is a clear difference around $E/p > 1.0$, which can be explained by the additional energy deposited by the annihilation of the antiproton in the calorimeter that is modeled well only in FTFP_BERT. This is also explored with data using identified antiprotons in Section 8.3.

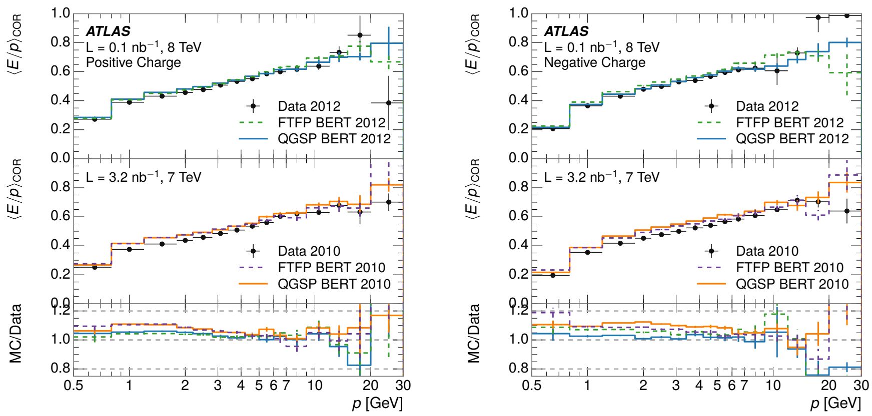

(a) (b)

Figure 9: Comparison of the $\langle E/p \rangle_{\mathrm{COR}}$ for (a) positive and (b) negative tracks as a function of track momentum for tracks with $|\eta| < 0.6$.

The $\langle E/p \rangle$ results in previous sections have considered the electromagnetic and hadronic calorimeters together as a single energy measurement, to emphasize the total energy deposited for a given particle. However, the deposits in each

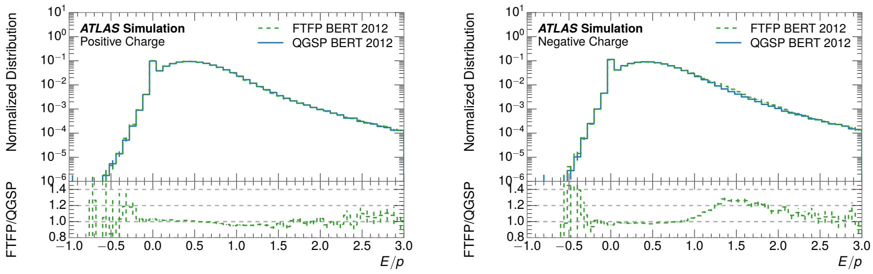

(a) (b)

Figure 10: Comparison of the E/p distributions for (a) positive and (b) negative tracks with $0.8 < p/\text{GeV} < 1.2$ and $|\eta| < 0.6$, in simulation with the `FTFP_BERT` and `QGSP_BERT` physics lists.

calorimeter are available separately and $\langle E/p \rangle$ can be constructed for each layer. As the layers are composed of different materials and are modeled separately in the detector geometry, confirmation that the simulation matches the data well in each layer adds confidence in both the description of hadronic interactions with the two different materials and also the geometric description of each.

The technique discussed in Section 8.2.3 for selecting minimally ionizing particle (MIP)s in the electromagnetic calorimeter is also useful in studying deposits in the hadronic calorimeter. Those MIPs deposit almost all of their energy exclusively in the hadronic calorimeter. Figure 11 shows $\langle E/p \rangle^{\text{Had}}_{\text{RAW}}$, where RAW indicates that no correction has been applied for neutral backgrounds and Had indicates that only clusters for the hadronic calorimeter are included. The RAW and COR versions of $\langle E/p \rangle$ in this case are the same, as the neutral background is negligible in that calorimeter layer. The distributions are shown both for the original EM scale calibration and after LCW calibration. The data and simulation agree very well in this comparison, except in the lowest momentum bin which has 5% discrepancy that has already been seen in similar measurements.

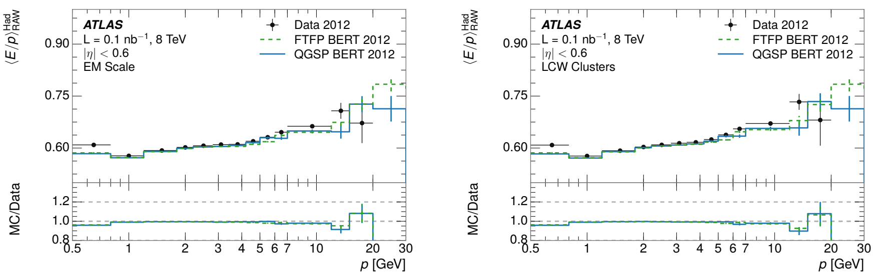

(a) (b)

Figure 11: Comparison of the response of the hadronic calorimeter as a function of track momentum (a) at the EM-scale and (b) after the LCW calibration.

A similar comparison can be made in the electromagnetic calorimeter by selecting particles which have no associated energy in the hadronic calorimeter. These results are measured in terms of $\langle E/p \rangle^{\text{EM}}_{\text{COR}}$, where EM designates that only clusters in the electromagnetic calorimeter are included and COR designates that the neutral background is subtracted as the neutral background is present in this case. Figure 12 shows the analogous comparisons to Figure 11 in the electromagnetic calorimeter. In this case the disagreement between data and simulation is more pronounced, with discrepancies as high as 5% over a larger range of momenta. This level of discrepancy indicates that the description of the electromagnetic calorimeter is actually the dominant source of discrepancy in the combined distributions in Section 8.2.4.

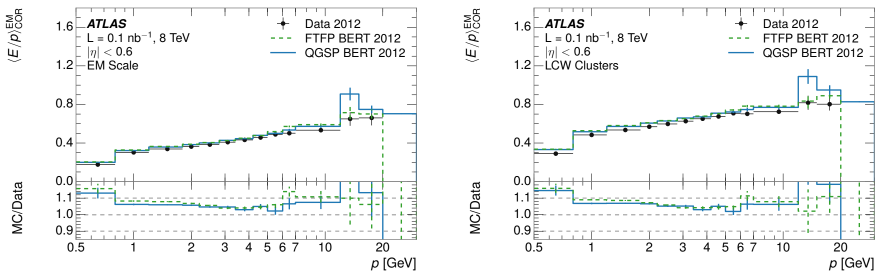

(a) (b)

Figure 12: Comparison of the response of the EM calorimeter as a function of track momentum (a) at the EM-scale and (b) with the LCW calibration.

NOTE: There are more studies that I skipped for brevity that could be included if interesting. E/p at different cluster threshold settings, E/p with pileup, E/p with cells. I also left out a lot of eta bins that appear in the paper so that this section didn't turn into 20 pages of plots.

8.3 IDENTIFIED PARTICLE RESPONSE

The inclusive response measurement for hadrons can be augmented by measuring the response for specific particle species. The simulation models each particle type separately, and understanding the properties of each is important in constraining the uncertainty on jets. In order to select and measure specific hadrons, this section relies on the displaced decays of long-lived particles. Such decays can be identified by reconstructing secondary vertices with a requirement on mass. In particular, Λ, $\bar{\Lambda}$, and K^0_S can be used to select a pure sample of protons, antiprotons, and pions, respectively.

8.3.1 DECAY RECONSTRUCTION

The measurement of response for identified particles uses the same selection as for inclusive particles (Section 8.1.3) with a few additions. Each event used is required to have at least one secondary vertex, and the tracks are required to match to that vertex rather than the primary vertex. Pions are selected from decays of $K^0_S \to \pi^+\pi^-$, which is the dominant decay for K^0_S to charged particles. Protons are selected from decays of $\Lambda \to \pi^- p$ and antiprotons from $\bar{\Lambda} \to \pi^+ \bar{p}$, which are similarly the dominant decays of Λ and $\bar{\Lambda}$ to charged particles. The species of parent hadron in these decays is determined by reconstructing the mass of the tracks associated to the secondary vertex. The sign of the higher momentum decay particle can distinguish between Λ and $\bar{\Lambda}$, which of course have the same mass, as the proton or antiproton is kinematically favored to have higher momentum. Examples of the reconstructed masses used to select these decays are shown in Figure 13.

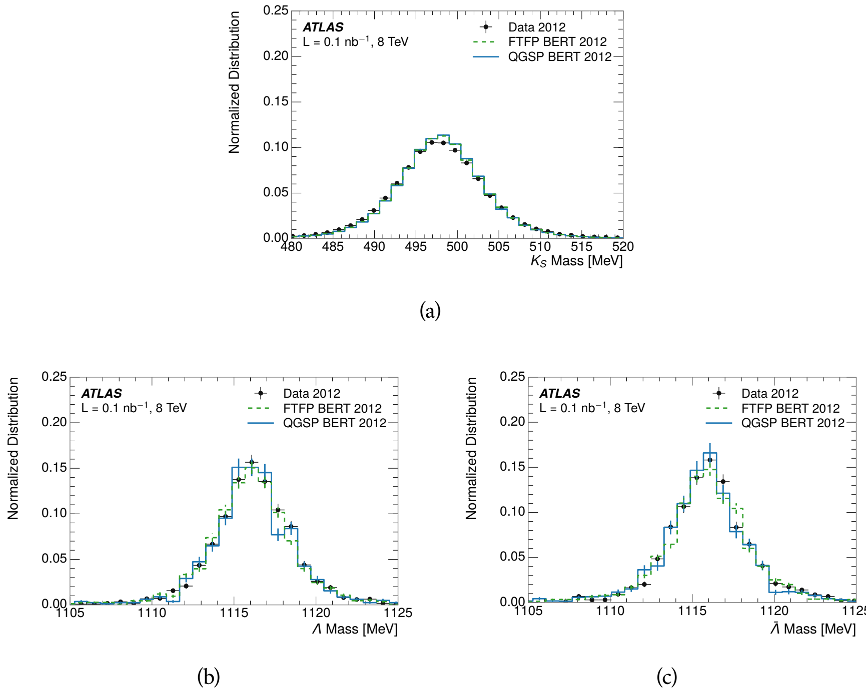

Figure 13: The reconstructed mass peaks of (a) K^0_S, (b) Λ, and (c) $\bar{\Lambda}$ candidates.

The dominant backgrounds for the identified particle decays are nuclear interactions and combinatoric sources. These are suppressed by the kinematic requirements on the tracks as well as an additional veto which removes candidates that are consistent with both a Λ or $\bar{\Lambda}$ and a K^0_S hypothesis, which is possible because of the different assumptions on particle mass in each case [5]. After these requirements, the backgrounds are found to be negligible compared to the statistical errors on these measurements.

8.3.2 IDENTIFIED RESPONSE

With these techniques the E/p distributions are extracted in data and simulation for each particle species and shown in Figure 14. These distributions are shown for a particular bin of E_a ($2.2 < E_a/\text{GeV} < 2.8$), rather than p. E_a is the energy available to be deposited in the calorimeter: for pions $E_a = \sqrt{p^2 + m^2}$, for protons $E_a = \sqrt{p^2 + m^2} - m$, and for antiprotons $E_a = \sqrt{p^2 + m^2} + m$. The features of the E/p distributions are similar to the inclusive case. There is a small negative tail from noise and a large fraction of tracks with zero energy from particles which do not reach the calorimeter. The long positive tail is noticeably more pronounced for antiprotons because of the additional energy generated by the annihilation in addition to the neutral background.

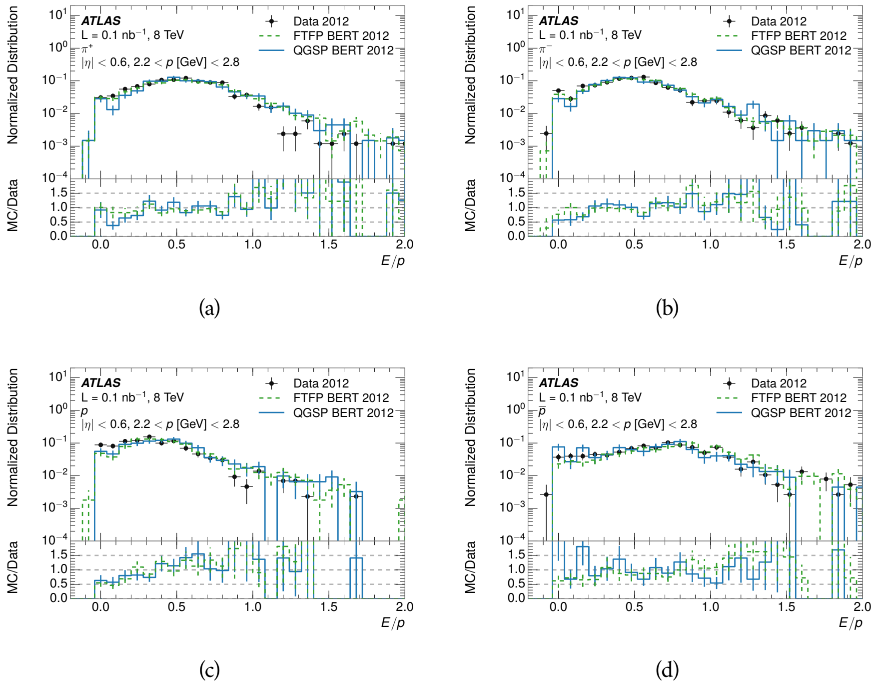

Figure 14: The E/p distribution for isolated (a) π^+, (b) π^-, (c) proton, and (d) anti-proton tracks.

The zero fraction is further explored in Figure 15 for pions and protons in data and simulation. The simulation consistently underestimates the zero fraction independent of particle species, which implies that this discrepancy is not caused by the model of a particular species but rather a feature common to all.

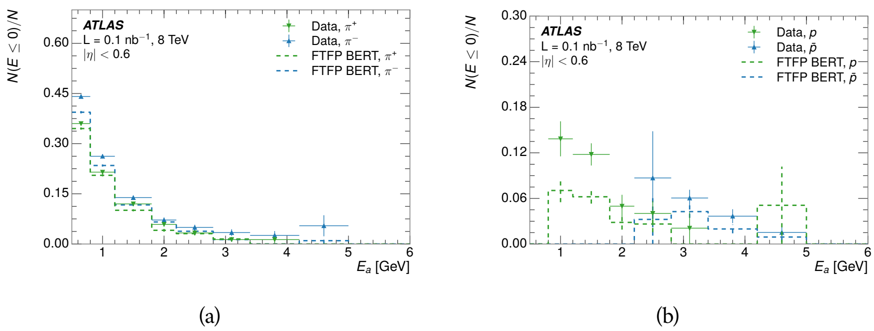

Figure 15: The fraction of tracks with $E \leq 0$ for identified (a) π^+ and π^-, and (b) proton and anti-proton tracks

It is also interesting to compare the response between the different particle species. One approach to do this is to measure the difference in $\langle E/p \rangle$ between two types, which has the advantage of removing the neutral background. These differences are shown in various combinations in Figure 16. The response for

π^+ is greater on average than the response to π^- because of a charge-exchange effect which causes the production of additional neutral pions in the showers of π^+ [27]. The response for π^+ is also greater on average than the response to p, because a large fraction of the energy of π^+ hadrons is converted to an electromagnetic shower [28, 29]. However, the $\bar{p}$ response is significantly higher than the response to π^- because of the annihilation of the antiproton. FTFP_BERT does a better job of modeling this effect than QGSP_BERT because of their different descriptions of $\bar{p}$ interactions with material.

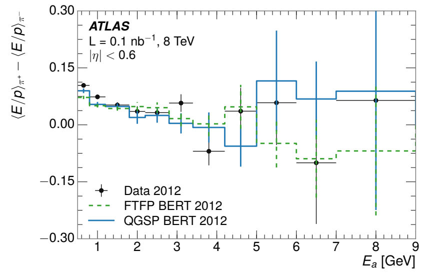

(a)

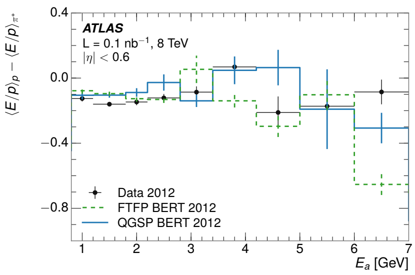

(b)

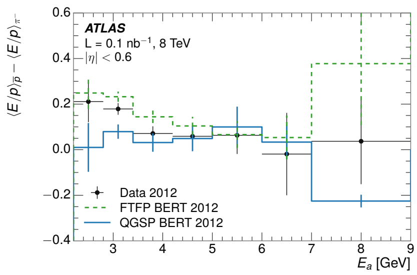

(c)

Figure 16: The difference in $\langle E/p \rangle$ between (a) π^+ and π^- (b) p and π^+, and (c) $\bar{p}$ and π^-.

It is also possible to remove the neutral background from these response distributions using the same technique as in Section 8.2.3. The technique is largely independent of the particle species and so can be directly applied to $\langle E/p \rangle$ for pions. The $\langle E/p \rangle_{\mathrm{COR}}$ distributions for pions are shown in Figure 17, which are very similar to the inclusive results. The inclusive hadrons are comprised mostly of pions, so this similarity is not surprising. It is also possible to see the small differences between π^+ and π^- response here, where $\langle E/p \rangle_{\mathrm{COR}}$ is higher on average for π^+. The agreement between data and simulation is significantly worse for the π^- distributions than for the π^+, with a discrepancy greater than 10% below 2-3 GeV.

8.3.3 ADDITIONAL SPECIES IN SIMULATION

The techniques above provide a method to measure the response separately for only pions and protons. However the hadrons which forms jets include a number of additional species such as kaons and neutrons. The charged kaons are

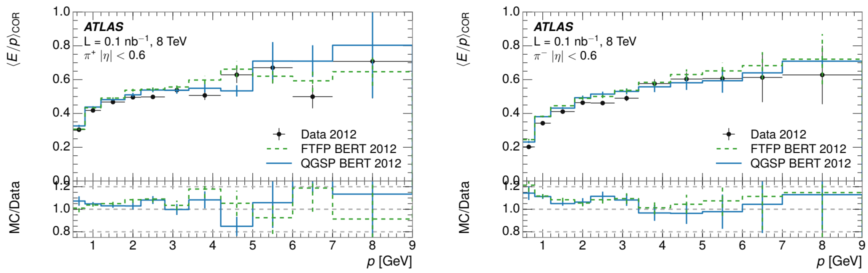

(a) (b)

Figure 17: $\langle E/p \rangle_{\mathrm{COR}}$ as a function of track momentum for (a) π^+ tracks and (b) π^- tracks.

an important component of the inclusive charged hadron distribution, which is comprised of roughly 60-70% pions, 15-20% kaons, and 5-15% protons. These are difficult to measure in data at the ATLAS detector, although a template subtraction technique has been proposed which may be effective with larger sample sizes [4]. The simulation of these particles includes noticeable differences in response at low energies, which are shown in Figure 18 for FTFP_BERT. The significant differences in response between low energy protons and antiprotons are accounted for above in the definitions of E_a.

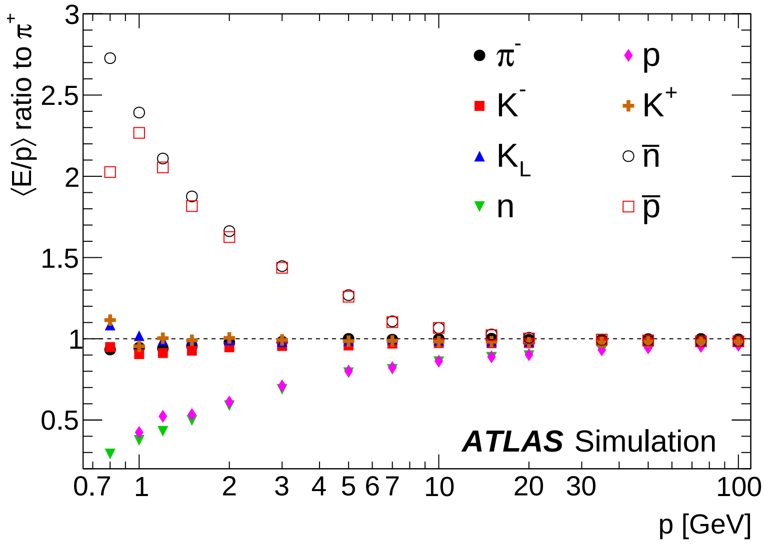

Figure 18: The ratio of the calorimeter response to single particles of various species to the calorimeter response to π^+ with the physics list FTFP_BERT.

8.4 SUMMARY

These various measurements of calorimeter response shown above for data and simulation illuminate the accuracy of the simulation of hadronic interactions at the ATLAS detector. The results were done using 2010 and 2012 data at 7 and 8

TeV, but reflect the most current understanding of the detector alignment and geometry. A number of measurements focusing on a comparison between protons and antiprotons suggest that FTFP_BERT models those interaction more accurately than QGSP_BERT. These measurements, among others, were the motivation to switch the default Geant4 simulation from FTFP_BERT to QGSP_BERT for all ATLAS samples.

Even with these updates, there are a number of small, approximately 5%, discrepancies in response between the data and simulation at low energies. At higher energies the simulation of hadronic interactions is very consistent with data. Chapter 9 discusses how to use these observed differences to constrain the jet energy scale and its associated uncertainties.

9 JET ENERGY RESPONSE AND UNCERTAINTY

9.1 MOTIVATION

As jets form a major component of many physics analyses at ATLAS, it is crucial to carefully calibrate the measurement of jet energies and to derive an uncertainty on that measurement. These uncertainties have often been the dominant systematic uncertainty in high-energy analyses at the Large Hadron Collider (LHC). Dijet and multijet balance techniques provide a method to constrain the JES and its uncertainty in data, and provide the default values used for ATLAS jet measurements at most energies [30]. These techniques are limited by their reliance on measuring jets in data, so they are statistically limited in estimating the jet energy scale at the highest jet energies. This chapter presents another method for estimating the jet energy scale and its uncertainty which builds up a jet from its components and thus can be naturally extended to high jet momentum. Throughout this chapter the jets studied are simulated using `Pythia8` with the CT10 parton distribution set [31] and the AU2 tune [8], and corrections are taken from the studies including data and simulation in Chapter 8.

As described in Section 7.2, jets are formed from topological clusters of energy in the calorimeters using the anti-k_t algorithm. These clusters originate from a diverse spectrum of particles, in terms of both species and momentum, leading to significantly varied jet properties and response between jets of similar produced momentum. Figure 19 shows the simulated distribution of particles within jets at a few examples energies. The E/p measurements provide a thorough understanding of the dominant particle content of jets, the charged hadrons.

9.2 UNCERTAINTY ESTIMATE

Simulated jets are not necessarily expected to correctly model the energy deposits in the calorimeters, because of the various discrepancies discussed in Chapter 8. To evaluate a jet energy response, the simulated jet energies are compared to a corrected jet built up at the particle level. Each cluster in a jet is associated to the truth particle which deposited it, and the energy in that cluster is then corrected for a number of effects based on measurements in data. The primary corrections come from the single hadron response measurements in addition to response measured using the combined test beam which covers higher momentum particles [32]. These corrections include both a shift (Δ), in order to make the simulation match the average response in data, and an uncertainty (σ) associated with the ability to constrain the difference between data and simulation. Some of the dominant sources of uncertainty are itemized in Table 1 with typical values, and the full list considered is described in detail in the associated

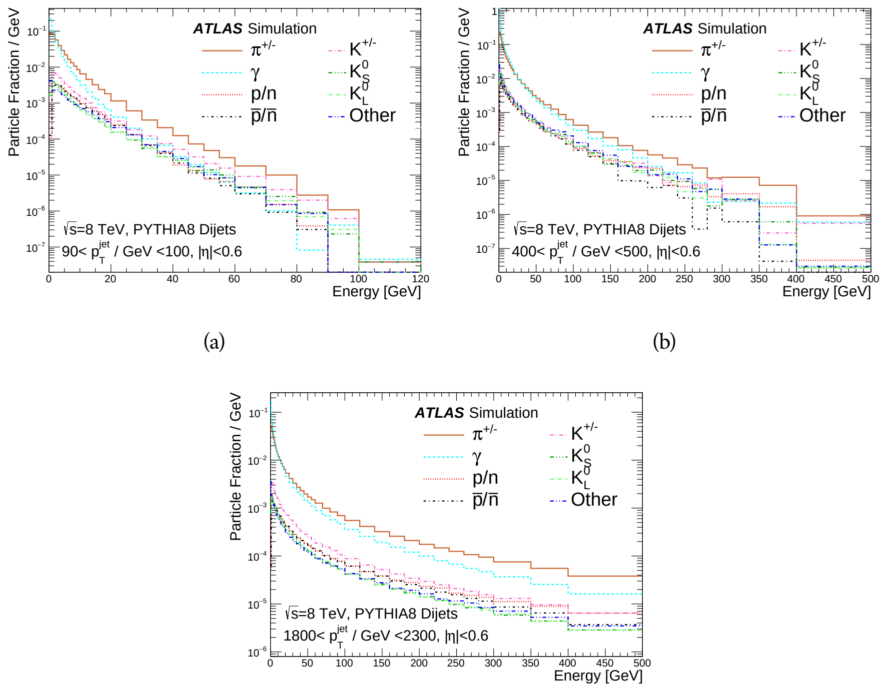

(a) (b) (c)

Figure 19: The spectra of true particles inside anti-k_t, $R = 0.4$ jets with (a) $90 < p_{\mathrm{T}}/\mathrm{GeV} < 100$, (b) $400 < p_{\mathrm{T}}/\mathrm{GeV} < 500$, and (c) $1800 < p_{\mathrm{T}}/\mathrm{GeV} < 2300$.

paper [4]. These uncertainties cover differences between the data and simulation in the modeling of calorimeter response to a given particle. No uncertainties are added for the difference between particle composition of jets in data and simulation.

From these terms, the jet energy scale and uncertainty is built up from individual energy deposits in simulation. Each uncertainty term is treated independently, and are taken to be gaussian distributed. The resulting scale and uncertainty is shown in Figure 20, where the mean response is measured relative to the calibrated energy reported by simulation. The dominant uncertainties come from the statistical uncertainties on the E/p measurements at lower energies and the additional uncertainty for out of range measurements at higher energies. The total uncertainty from this method at intermediate jet energies is comparable to other simulation-based methods [33] and is about twice as large as in-situ methods using data [30]. This method is the only one which provides an estimation above 1.8 TeV, however, and so is still a crucial technique in analyses that search for very energetic jets.

These techniques can also be used to measure the correlation between bins of average reconstructed jet momentum across a range of p_T and $|\eta|$, where correlations are expected because of a similarity in particle composition at similar energies. Figure 21 shows these correlations, where the uncertainties on jets in neighboring bins are typically between 30% and 60% correlated. The uncertainty on all jets becomes significantly correlated at high energies and larger pseudora-

Abbrev.	Description	Δ (%)	σ (%)
In situ E/p	The comparison of $\langle E/p \rangle_{\mathrm{COR}}$ as described in Chapter 8 with statistical uncertainties from 500 MeV to 20 GeV.	0-3	1-5
CTB	The main $\langle E/p \rangle$ comparison uncertainties, binned in p and $\lvert\eta\rvert$, as derived from the combined test beam results, from 20 to 350 GeV [32].	0-3	1-5
E/p Zero Fraction	The difference in the zero-fraction between data and MC simulation from 500 MeV to 20 GeV.	5-25	1-5
E/p Threshold	The uncertainty in the EM calorimeter response from the potential mismodeling of threshold effects in topological clustering.	0	0-10
Neutral	The uncertainty in the calorimeter response to neutral hadrons based on studies of physics model variations.	0	5-10
K_{L}	An additional uncertainty in the response to neutral K_L in the calorimeter based on studies of physics model variations.	0	20
E/p Misalignment	The uncertainty in the p measurement from misalignment of the ID.	0	1
Hadrons, $p > 350$ GeV	A flat uncertainty for all particles above the energy range or outside the longitudinal range probed with the combined test beam.	0	10

Table 1: The dominant sources of corrections and systematic uncertainties in the JES estimation technique, including typical values for the correcting shift (Δ) and the associated uncertainty (σ).

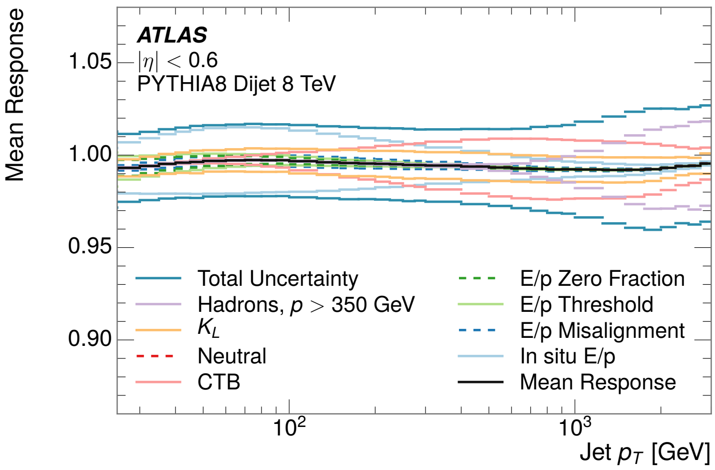

(a)

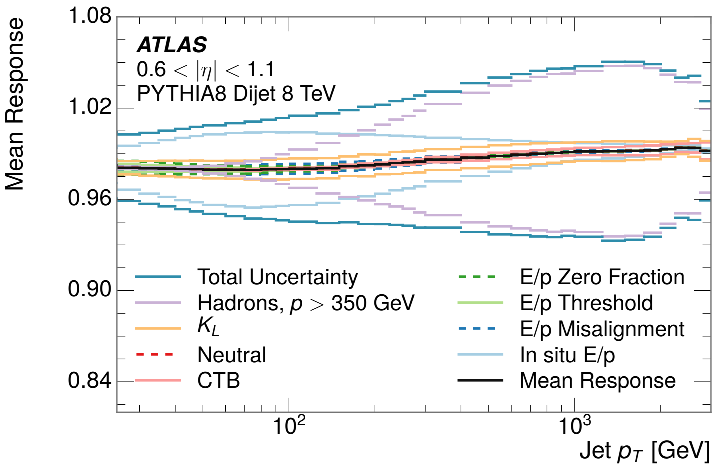

(b)

Figure 20: The JES uncertainty contributions, as well as the total JES uncertainty, as a function of jet p_T for (a) $|\eta| < 0.6$ and (b) $0.6 < |\eta| < 1.1$.

pidities, when the uncertainty becomes dominated by the single term reflecting out of range particles.

9.3 SUMMARY

The technique described above provides a jet energy scale and uncertainty by building up jet corrections from the energy deposits of constituent particles. The E/p measurements are crucial in providing corrections for the majority of particles in the jets. The uncertainty derived this way is between 2 and 5% and is about twice as large at corresponding momentum than jet balance methods. However this is the only uncertainty available for very energetic jets using 2012 data and simulation, and repeating this method with Run 2 data and simulation will be

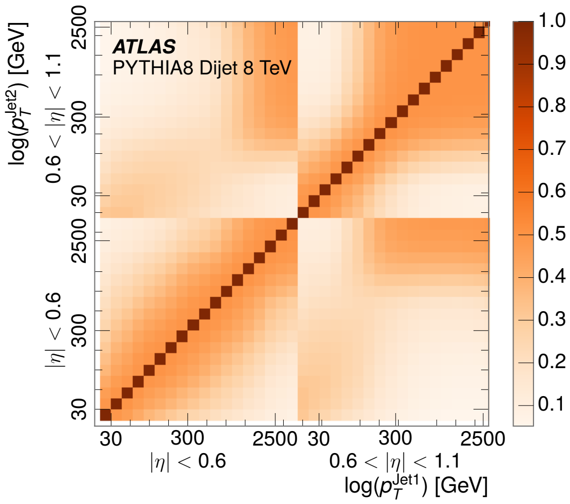

Figure 21: The JES correlations as a function of jet p_{T} and $|\eta|$ for jets in the central region of the detector.

807 important in providing an uncertainty for the most energetic jets in 13 TeV col-
808 lisions.

PART V

SEARCH FOR LONG-LIVED PARTICLES

You can put some informational part preamble text here.

10

LONG-LIVED PARTICLES IN ATLAS

10.1 OVERVIEW AND CHARACTERISTICS

10.2 SIMULATION

11 EVENT SELECTION

The Long-Lived Particles (LLPs) targeted by this search differ in their interactions with the detector from SM particles primarily because of their large mass. When produced at the energies available at the LHC, that large mass results in a low β and such slow-moving particles heavily ionize in detector material. Each layer of the pixel detector provides a measurement of that ionization, through time over threshold (ToT), as discussed in Section 6.3.1. The ionization in the pixel detector, quantified in terms of dE/dx, provides the major focus for this search technique, both for its discriminating power and also because of the large range of lifetimes where it can be used. The dE/dx variable needs to be augmented with a few additional selection requirements to form a complete search.

Ionization is not currently available in any form during triggering, so this search instead relies on E_T^{miss} to trigger signal events. Although triggering on E_T^{miss} is not particularly efficient, E_T^{miss} is often large for many production mechanisms of LLPs, as discussed in Section 10.1.

Ionization is most effective in rejecting backgrounds for well-measured, high-momentum tracks, so some basic requirements on quality and kinematics are placed on the particles considered in this search. In particular a newly introduced tracking variable is very effective in removing highly-ionizing backgrounds caused by overlapping tracks. A few additional requirements are placed on the tracks considered for LLP candidates that increase background rejection by targeting specific types of SM particles. These techniques provide a significant analysis improvement over previous iterations of ionization-based searches on ATLAS by providing additional background rejection with minimal loss in signal efficiency.

The ionization measurement with the Pixel detector can be calibrated to provide an estimator of $\beta\gamma$. That estimate, together with the momentum measurement provided by tracking, can be used to reconstruct a mass for each track which traverses the pixel detector. That mass variable will be peaked at the LLP mass for any signal, and provides an additional tool to search for an excess. In addition to an explicit requirement on ionization, this search constructs a mass-window for each targeted mass range in order to evaluate any excess of events and to set limits.

The strategy discussed here is optimized for lifetimes of $O(1)$ - $O(10)$ ns. Pixel ionization is especially useful in this regime as particles only need to propagate through the first seven layers of the inner detector, about 37 cm from the beam axis. The search is still competitive with other searches for LLPs at longer lifetimes, because the primary discriminating variables are still applicable even for particles that do not decay within the detector [34]. Although the basic strategy remains the same for all lifetimes, two signal regions are defined to optimize separately for intermediate and long lifetime particles.

11.1 TRIGGER

Triggering remains a significant difficulty in defining an event selection with high signal efficiency in a search for LLPs. There are no triggers available in the current ATLAS system that can fire directly from a high momentum track with large ionization (Section 6.6). Although in some configurations a charged LLP can fire muon triggers, this requirement introduces significant model dependence on both the allowed lifetimes and the interactions in the calorimeter [35].

For a search targetting particles which may decay prior to reaching the muon system, the most efficient available trigger is based on missing energy [35]. As discussed in Section 10.1, signal events can produce E_T^{miss} by two primary mechanisms. The decays of R-Hadrons to neutralinos can produce missing energy when the neutralinos go undetected in the calorimeters. LLPs which do not decay before the calorimeters also can produce missing energy because they do not deposit much energy. Either case to some extent relies on kinematic degrees of freedom to produce missing energy, as the pair-produced LLPs tend to balance each other in the transverse plain. That balance results in a relatively low efficiency for long-lifetime particles, roughly 40%, and efficiencies between 65% and 95% for shorter lifetimes depending on both the mass and the lifetime.

11.2 KINEMATICS AND ISOLATION

After the trigger requirement, each event is required to have a primary vertex reconstructed from at least two well-measured tracks in the inner detector, each with $p_{\text{T}} > 400$ MeV. If more than one such vertex exists, the primary vertex is taken to be the one with the largest summed track momentum for all tracks associated to that vertex. The offline reconstructed E_T^{miss} is required to be above 130 GeV to additionally reject SM backgrounds. The transverse missing energy is calculated using fully reconstructed and calibrated offline objects, as described in Section 7.5. In particular the E_T^{miss} definition in this selection uses jets reconstructed with the anti-k_t algorithm with radius $R = 0.4$ from clusters of energy in the calorimeter (Section 7.2) and with $p_T > 20$ GeV, as well as reconstructed muons, electrons, and tracks not identified as another object type.

The E_T^{miss} distributions are shown for data and a few simulated signals in Figure 22, after the trigger requirement. The cut placed at 130 GeV is 95% efficient for metastable and 90% efficient for stable particles, because of the missing energy generating mechanisms discussed previously. The distribution of data in this figure and subsequent figures in this section can be interpreted as the distribution of backgrounds, as any signal contamination would be negligible if present at these early stages of the selection (prior to the final requirement on mass). The background falls rapidly with missing energy, motivating the direct requirement on E_T^{miss} for the signal region. Although a tigher requirement than the specified value of 130 GeV would seem to increase the search potential from these early distributions, other requirements are more optimal when taken as a whole. The specific values for each requirement in signal region were optimized considering the increase in discovery reach for tightening the requirement on each discriminating variable. **NOTE: Is it interesting to discuss the signal region optimization process in detail? I could add another section on how the values were determined, although in truth it is at least partially historical precedence.**

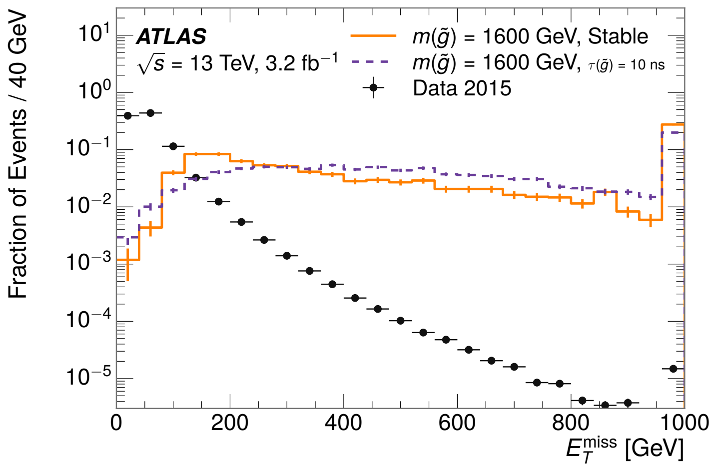

Figure 22: The distribution of E_T^{miss} for data and simulated signal events, after the trigger requirement.

Potential signal events are then required to have at least one candidate LLP track. Although the LLPs are produced in pairs, many models do not consistently yield two charged particles. For example, in the R-Hadron model highlighted here, only 20% of events have two charged R-Hadrons while 47% of events have just one. A signal region requiring two charged candidates could be a powerful improvement in background rejection for a larger dataset, but it is not considered in this version of the analysis as it was found to be unnecessary to reject the majority of backgrounds.

For a track to be selected as a candidate, it must have $p_T > 50$ GeV and pass basic quality requirements. The track must be associated to the primary vertex. It must also have at least seven clusters in the silicon layers in the inner detector to ensure an accurate measurement of momentum. Those clusters must include one in the innermost layer if the extrapolated track is expected to pass through that layer. And to ensure a reliable measurement of ionization, the track is required to have at least two clusters in the pixel detector that provide a measurement of dE/dx.

At this point in the selection, there is a significant high-ionization background from multiple tracks that significantly overlap in the inner detector. Previous version of this analysis have rejected these overlaps by an explicit overlap rejection between pairs of fully reconstructed tracks, typically by requiring no additional tracks within a cone around the candidate. This technique, however, fails to remove the background from tracks that overlap so precisely that the tracks cannot be separately resolved.

A new method, added in Run 2, identifies cluster shapes that are likely formed by multiple tracks based on a neural network classification algorithm. The number of clusters that are classified this way in the pixel detector for a given track is called N_{split}. As the shape of clusters requires significantly less spatial separation to identify overlaps than it does to reconstruct two fully resolved tracks, this variable is more effective at rejecting backgrounds from overlaps. Figure 23 shows the dependence of ionization on N_{split}; as N_{split} increases the mean of dE/dx grows significantly up to twice the expected value when $N_{\text{split}} = 4$.

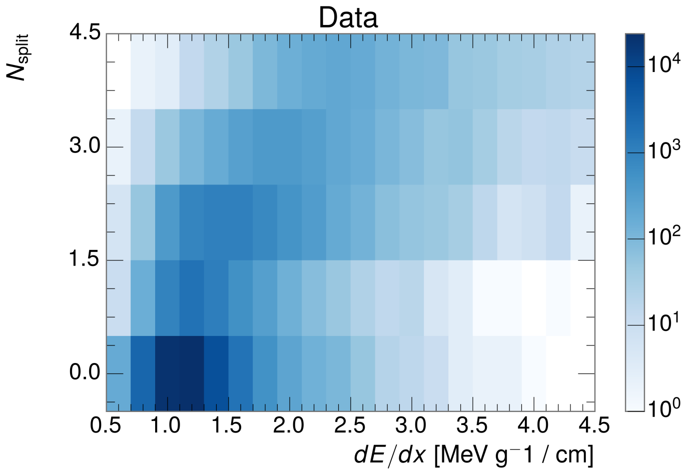

Figure 23: The dependence of dE/dx on N_{split} in data after basic track hit requirements have been applied.

This requirement is very succesful in reducing the long positive tail of the dE/dx distributions, as can be seen in Figure 24. Comparing the distribution for "baseline tracks", tracks with only the above requirements on clusters applied and before the requirement on N_{split}, to the distribution with $N_{\text{split}} = 0$, it is clear that the fraction of tracks with large dE/dx is reduced be several orders of magnitude. The isolated tracks are very close to the dE/dx distribution of identified muons, which are extremely well isolated on average. Figure 24 also includes the distribution of dE/dx in an example signal simulation to demonstrate how effective dE/dx is as a discriminating variable with this isolation applied. The background falls rapidly for $dE/dx > 1.8$ MeVg^{-1}cm^2 while the majority of the signal, approximately 90% depending on the mass, falls above that threshold. Over 90% of LLP tracks in simulated signal events pass the N_{split}-based isolation requirement.

A few additional kinematic requirements are imposed to help reduce SM backgrounds. The momentum of the candidate track must be at least 150 GeV, and the uncertainty on that measurement must be less than 50%. The distribution of momentum is shown in Figure 25 for tracks in data and simulated signal events after the previously discussed requirements on clusters, transverse momentum, and isolation have been imposed. The signal particles are much harder on average than their backgrounds because of the high energy interactions required to produce them. The transverse mass, M_{T}, defined as

$$M_{\text{T}} = \sqrt{2 p_{\text{T}} E_T^{\text{miss}} (1 - \cos(\Delta\phi(E_T^{\text{miss}}, \text{track})))} \quad (1)$$

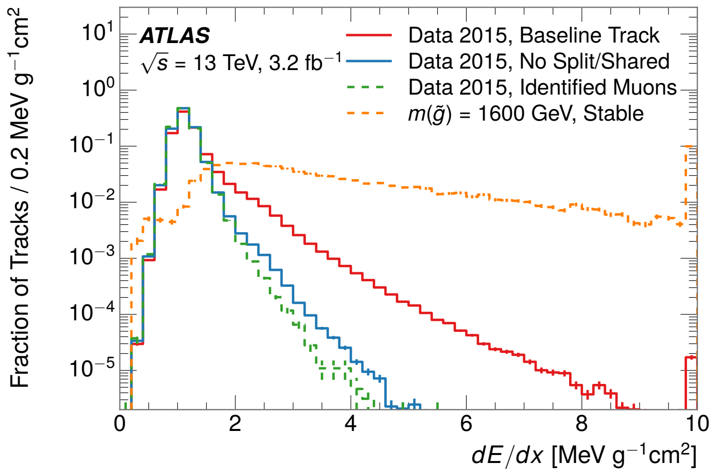

Figure 24: The distribution of dE/dx with various selections applied in data and simulated signal events.

957 estimates the mass of a decay of to a single charged particle and an undetected
958 particle and is required to be greater than 130 GeV to reject contributions from
959 the decay of W bosons. Figure 26 shows the distribution of M_{T} for data and
960 simulated signal events. The signal is distributed over a wide range of M_{T}, with
961 about 90% above the threshold value of 130 GeV. The data shows a dual-peaked
962 structure, where the first peak comes from W boson decays and the second peak
963 is a kinematic shaping from the requirements on E_T^{miss} and the track p_{T} in dijet
964 events.

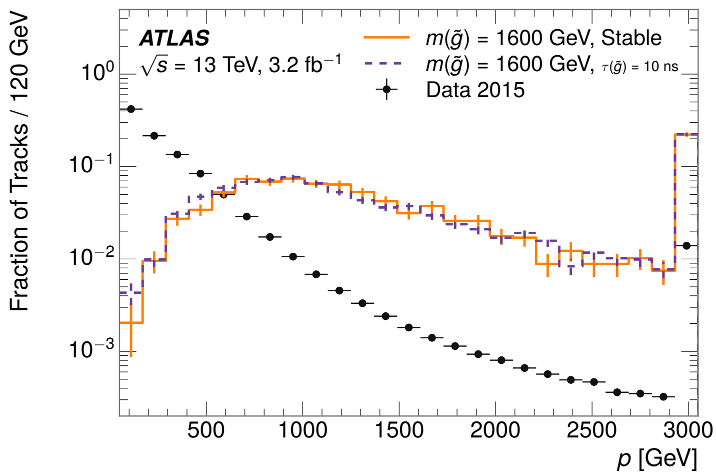

Figure 25: The distribution of track momentum for data and simulated signal events, after previous selection requirements have been applied.

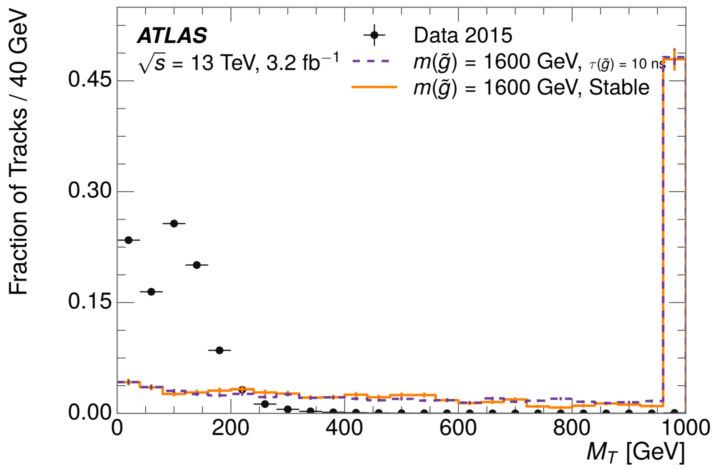

Figure 26: The distribution of M_T for data and simulated signal events, after previous selection requirements have been applied.

11.3 STANDARD MODEL REJECTION

Because the search selects events with just a single, highly-ionizing track, backgrounds can be formed by a wide variety of SM processes when various charged particles have a few randomly large deposits of energy in the pixel detector. Those backgrounds can be effectively rejected by targeting the types of particles produced rather than the processes which produce them, as LLPs will have significant differences compared to any SM particle. These rejections focus on using additional features of the event, other than the kinematics or ionization of the candidate track, as it provides a powerful source of background rejection with very high signal efficiency. The lifetime of the particle can significantly change its detector characteristics, as discussed in Section 10.1. To accomodate these differences, the SM rejections defined in this section are split to form two signal regions, one for long-lifetimes particles, the "stable" region, and one for intermediate lifetime particles, the "metastable" region.

Jets can be very effectively rejected by considering the larger-scale isolation of the candidate track. In this case the isolation focuses on the production of nearby particles as a jet-veto, rather than isolation from overlapping tracks to reduce high-ionization backgrounds. As explained in Section 10.1, the fragmentation process which produces an R-Hadron is very hard and thus is not expected to produce additional particles. The jet-veto uses the summed momentum of tracks with a cone of $\Delta R < 0.25$, referred to as p_T^{Cone}, which is shown in Figure 27 for data and simulated signal events. In the data this value has a peak at zero from isolated tracks such as leptons, and a long tail from jets which contains as much as 80% of the background above 20 GeV at this stage of the selection. In signal events $p_T^{\text{Cone}}$is strongly peaked at zero and significantly less than 1% is above 20 GeV. This makes a requirement of $p_T^{\text{Cone}} < 20$ GeV one of the most effective methods to reject background without losing signal efficiency. For the stable signal region, this cut is further tightened to $p_T^{\mathrm{Cone}} < 5$ GeV as it is the most effective variable remaining to extend the search reach for long lifetimes.

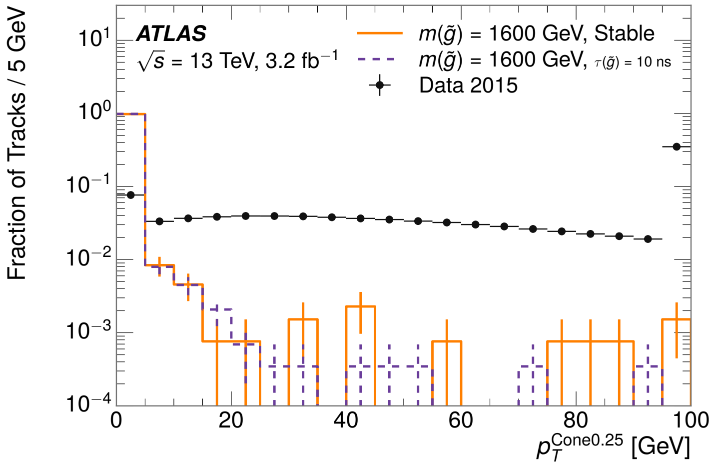

Figure 27: The distribution of summed tracked momentum within a cone of $\Delta R < 0.25$ around the candidate track for data and simulated signal events, after previous selection requirements have been applied.

Even for fully isolated particles, there are additional methods to reject each type of particle using information in the muon system and calorimeters. Muons can be identified very reliably using the tracks in the muon system, as described in Section 7.4. For intermediate lifetimes the LLPs do not survive long enough to reach the muon system, and so muons are vetoed by rejecting tracks that associate to a muon with medium muon identification requirements. For longer lifetimes, this rejection is not applied because LLPs which reach the muon system can be identified as muons as often as 30% of the time in simulated samples.

Calorimeter-based particle rejection relies on the expected small deposits of energy from LLPs. When the lifetime is long enough to reach the calorimeter, a LLP deposits little of its energy as it traverses the material, as discussed in Section 10.1. Even when the particle does decay before the calorimeter, the majority of its energy is carried away by the Lightest Supersymmetric Particle (LSP) and not deposited in the calorimeter. In both cases the energy is expected to be distributed across the layers of the calorimeters and not peaked in just one layer. This can be quantified in terms of E/p, the ratio of calorimeter energy of a nearby jet to the track momentum, and f_{EM}, the fraction of energy in that jet within the electromagnetic calorimeter. When no jets fall within a cone of 0.05 of the particle, E/p and $f_{\mathrm{EM}}$are both defined as zero. E/p is expected to be above 1.0 for typical SM particles because of calibration and the contributions from other nearby particles. At these momenta there is no significant zero fraction due to interactions with the detector or insuffficent energy deposits (see Section 8.2.2). $f_{\mathrm{EM}}$is peaked close to 1.0 for electrons, and distributed between 10% and 90% for hadrons.

These trends can be seen in the two dimensional distribution for signal in Figure 28 for stable and metastable (10 ns) events. The majority of R-Hadrons in both samples fall into the bin for $E/p = 0$ and $f_{\mathrm{EM}} = 0$ because the majority of the time there is no associated jet. In the stable sample, when there is an associated jet, E/p is typically still below 0.1, and the $f_{\mathrm{EM}}$is predominantly under 0.8. In the metastable sample, on the other hand, E/p is larger but still typically below 0.1 because of actual jets produced during the decay. The $f_{\mathrm{EM}}$is much lower on average in this case, below 0.1, because the 10 ns lifetime particles rarely decay before passing through the electromagnetic calorimeter. Figure 28 also includes simulated Z decays to electrons or tau leptons. From the decays to electrons it is clear that the majority of electrons have f_{EM}above 0.9. The tau decays include a variety of products. Muons can be seen in the bin where $E/p = 0$ and $f_{\mathrm{EM}} = 0$ because they do not have an associated jet. Electrons fall into the range where $E/p > 1$ and $f_{\mathrm{EM}} > 0.9$. Hadronic tau decays are the most common, and fall in the range of $0.1 < f_{\mathrm{EM}} < 0.9$ and $E/p > 1.0$.

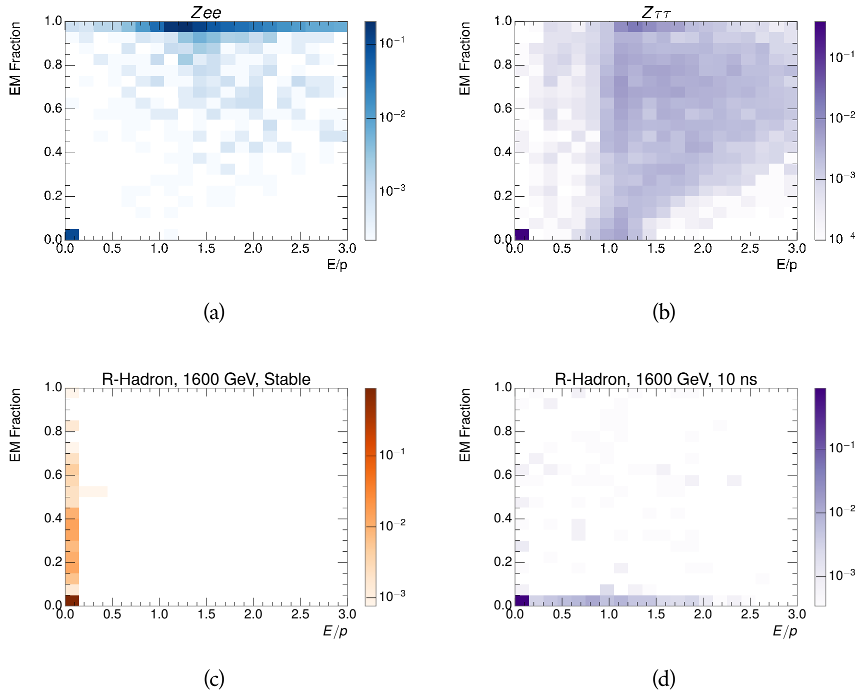

(a) (b) (c) (d)

Figure 28: The normalized, two-dimensional distribution of E/p and $f_{\mathrm{EM}}$for simulated (a) $Z \to ee$, (b) $Z \to \tau\tau$, (c) 1200 GeV Stable R-Hadron events, and (d) 1200 GeV, 10 ns R-Hadron events.

These differences motivate an electron rejection by requiring an f_{EM}below 0.9. Similarly, isolated hadrons are rejected by requiring $E/p < 1.0$. These requirements combine to remove the majority of isolated electrons and hadrons but retain over 95% of the simulated signal across a range of masses and lifetimes.

11.4 IONIZATION

The final requirements on the candidate track are the primary discriminating variables, the ionization in the pixel detector and the corresponding mass. That

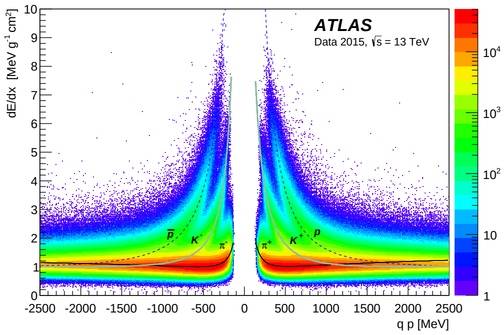

Figure 29: Two-dimensional distribution of dE/dx versus charge signed momentum (qp) for minimum-bias tracks. The fitted distributions of the most probable values for pions, kaons and protons are superimposed.

ionization is measured in terms of dE/dx, which was shown for data and simulated signal events in Figure 24. dE/dx is dramatically greater for the high mass signal particles than the backgrounds, which start to fall immediately after the minimally ionizing peak at 1.1 $\text{MeVg}^{-1}\text{cm}^2$. The dE/dx for candidate tracks must be greater than a pseudorapidity-dependent threshold, specifically $1.80 - 0.11|\eta| + 0.17\eta^2 - 0.05|\eta|^3$ MeV g^{-1} cm^{-2}, in order to correct for an approximately 5% dependence of the MIP peak on η. The requirement was chosen as part of the signal region optimization, and manages to reduce the backgrounds by a factor of 100 while remaining 70-90% efficient for simulated signal events depending on the mass.

11.4.1 MASS ESTIMATION

The mean value of ionization in silicon is governed by the Bethe-Bloch formula and the most probable value follows a Landau-Vavilov distribution [36]. Those forms inspire a parametric description of dE/dx in terms of $\beta\gamma$,

$$(dE/dx)_{\mathrm{MPV}}(\beta\gamma) = \frac{p_1}{\beta^{p_3}}\ln(1 + [p_2\beta\gamma]^{p_5}) - p_4 \tag{2}$$

which performs well in the range $0.3 < \beta\gamma < 1.5$. This range includes the expected range of $\beta\gamma$ for the particles targetted for this search, with $\beta\gamma \approx 2.0$ for lower mass particles (O(100 GeV)) and up to $\beta\gamma \approx 0.5$ for higher mass particles (O(1000 GeV)). The parameters, p_i, are fit using a 2015 data sample of low-momentum pions, kaons, and protons as described in Ref. [37]. Figure 29 shows the two-dimensional distribution of dE/dx and momentum along with the above fitted values for $(dE/dx)_{\mathrm{MPV}}$.

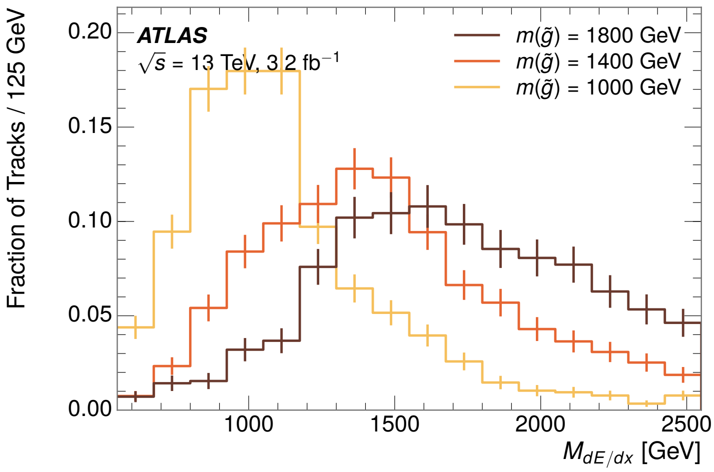

Figure 30: The distribution of mass estimated using dE/dx for simulated stable R-Hadrons with masses between 1000 and 1600 GeV.

The above equation (2) is then numerically inverted to estimate $\beta\gamma$ and then mass for each candidate track. In simulated signal events, the mean of this mass value reproduces the generated mass up to around 1800 GeV to within 3%, and 3% shift is applied to correct for this difference. The mass distributions prior to this correction are shown for a few stable mass points in Figure 30. The large widths of these distributions come from the high variability in energy deposits in the pixel detector, but the means converge to the expected values.

This analysis evaluates expected yields and the resulting cross sectional limits using windows in this mass variable. The windows are formed by fitting mass distributions like those in Figure 30 to Gaussian distribution and taking al events that fall within $\pm 1.4\sigma$ of the mean. As can be seen in Figure 30, typical values for this width are $\sigma \approx 300 - 500$ GeV depending on the generated mass.

11.5 EFFICIENCY

The numbers of events passing each requirement through ionization are shown in Table 2 for the full 2015 dataset and a simulated 1600 GeV, 10 ns lifetime R-Hadron sample. The table highlights the overall acceptance × efficiency for signal events, which for this example is 19%. Between SM rejection and ionization, this signal region reduces the background of tracks which pass the kinematic requirements down by an additional factor of almost 2000.

There is a strong dependence of this efficiency on lifetime and mass, with efficiencies dropping to under 1% at low lifetimes. Figure 31 shows the dependence on both mass and lifetime for all signal samples considered in this search. The dependence on mass is relatively slight and comes predominantly from the increasing fraction of R-Hadrons which pass the ionization cut with increasing mass. The trigger and E_T^{miss} requirements are most efficient for particles that decay before reaching the calorimeters. However, the chance of a particle to be

Selection	Exp. Signal Events	Observed Events in 3.2 fb^{-1}
Generated	26.0 ± 0.3	
E_T^{miss} Trigger	24.8 ± 0.3 (95%)	
$E_T^{\text{miss}} > 130$ GeV	23.9 ± 0.3 (92%)	
Track Quality and $p_{\text{T}} > 50$	10.7 ± 0.2 (41%)	368324
Isolation Requirement	9.0 ± 0.2 (35%)	108079
Track $p > 150$ GeV	6.6 ± 0.2 (25%)	47463
$M_{\text{T}} > 130$ GeV	5.8 ± 0.2 (22%)	18746
Electron and Hadron Veto	5.5 ± 0.2 (21%)	3612
Muon Veto	5.5 ± 0.2 (21%)	1668
Ionization Requirement	5.0 ± 0.1 (19%)	11

Table 2: The expected number of events at each level of the selection for metastable 1600 GeV, 10 ns R-Hadrons, along with the number of events observed in data, for 3.2 fb^{-1}. The simulated yields are shown with statistical uncertainties only. The total efficiency × acceptance is also shown for the signal.

reconstructed as a high-quality track decreases significantly at low lifetimes as the particle does not propagate sufficiently through the inner detector. These effects lead to a maximum in the selection efficiency for lifetimes around 10-30 ns.

The inefficiency of this signal region at short lifetimes comes almost exclusively from an acceptance effect, in that the particles do not reach the necessarily layers of the SCT. This can be seen more clearly by defining a fiducial region which includes events with at least one R-Hadron that is produced with non-zero charge, $p_{\text{T}} > 50$ GeV, $p > 150$ GeV, $|\eta| < 2.5$, and a decay distance greater than 37 cm in the transverse plane. At short (1 ns) lifetimes, the acceptance into this region is as low as 4%. Once this acceptance is accounted for, the selection efficiency ranges from 25% at lifetimes of 1 ns up to 45% at lifetimes of 10 ns.

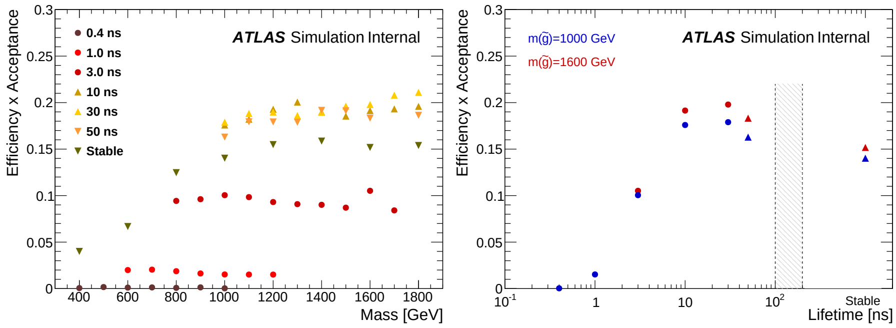

(a) (b)

Figure 31: The acceptance × efficiency as a function of R-Hadron (a) mass and (b) lifetime. (a) shows all of the combinations of mass and lifetime considered in this search, and (b) highlights the lifetime dependence for 1000 GeV and 1600 GeV R-Hadrons.

12

BACKGROUND ESTIMATION

The event selection discussed in the previous section focuses on detector signatures, emphasizing a single high-momentum, highly-ionizing track. That track is then required to be in some way inconsistent with the expected properties of SM particles, with various requirements designed to reject jets, hadrons, electrons, and muons (Section 11.3). So the background from this search comes entirely from reducible backgrounds that are outliers of various distributions like dE/dx, f_{EM}, and p_T^{Cone}. The simulation can be tuned in various ways to do an excellent job of modeling the average properties of each particle type [38], but it is not necessarily expected to accurately reproduce outliers. For these reasons, the background estimation used for this search is estimated entirely using data.

12.1 BACKGROUND SOURCES

Charged particles with lifetimes long enough to form tracks in the inner detector can be grouped into three major categories based on their detector interactions: hadrons, electrons, and muons. Every particle that enters into the background for this search belongs to one of these types. Relatively pure samples of each of these types can be formed in data by inverting the various rejection techniques in Section 11.3. Specifically, muons are selected requiring Medium muon identification, electrons requiring $E/p > 1.0$ and $f_{\text{EM}} > 0.95$, and hadrons requiring $E/p > 1.0$ and $f_{\text{EM}} < 0.95$.

Figure 32 shows the distributions of momentum and dE/dx for these categories in data, after requiring the event level selection as well as the track requirements on p_{T}, hits, and N_{split}, as discussed in Section 11.2. Simulated signal events are included for reference. These distribution are only illustrative of the differences between types, as the rejection requirements could alter their shape. This is especially significant for momentum which enters directly into E/p and can inderectly affect muon identification. However the various types show clear differences in both distributions. Momentum is expected to vary significantly because of the production mechanisms for the different species. **Note for Laura: Interesting that the momentum tail is so much higher for electrons than muons, any idea why that would happen?** dE/dx is different between types because of incomplete isolation; although the requirement on N_{split} helps to reduce the contribution of nearby particles it does not completely remove the effect of overlaps. Muons are better isolated and thus have the smallest fraction of dE/dx above the threshold of 1.8 $\text{MeVg}^{-1}\text{cm}^2$; hadrons and electrons have a larger fraction above this threshold.

It is difficult to determine what fraction of each particle type enters into the final signal region. The background method will not have significant dependence

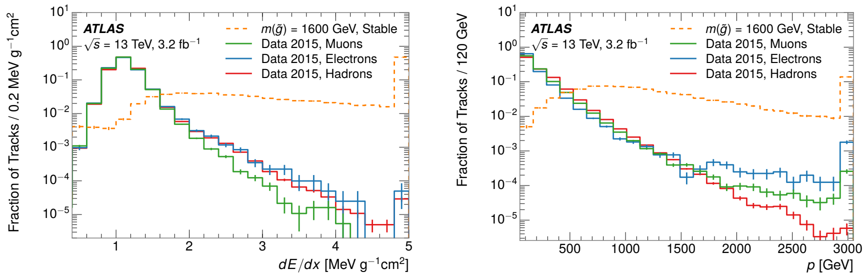

(a) (b)

Figure 32: The distribution of (a) dE/dx and (b) momentum for tracks in data and simulated signal after requiring the event level selection and the track selection on p_{T}, hits, and N_{split}. Each subfigure shows the normalized distributions for tracks classified as hadrons, electrons, and muons in data and R-Hadrons in the simulated signal.

on the relative contributions of each species, but it is useful to understand the differences between each when considering the various tests of the method.

12.2 PREDICTION METHOD

The data-driven background estimation relies on the independence of ionization and other aspects of the event. For standard model particles with momenta above 50 GeV, dE/dx is not correlated with momentum. So, the proposed method to estimate the mass distribution of the signal region is to use momentum from a track with low dE/dx (below the threshold value) and to combine it with a random dE/dx value from a dE/dx template. The resulting track is just as likely as the original, so a number of such random generations forms a distribution of mass for the signal region.

Algorithmically this method is implemented by forming two distinct Control Regions (CRs). The first CR, CR1, is formed by applying the entire event selection from Chapter 11 up to the dE/dx and mass requirements. The dE/dx requirement is instead inverted for this region. Because of the independence of dE/dx, the tracks in this control region have the same kinematic distribution as the tracks in the signal region, and are used to measure a two-dimensional template of p and η. The second CR, CR2, is formed from the event selection through the dE/dx requirement, but with an inverted E_T^{miss} requirement. The tracks in this control region are expected to have similar dE/dx distributions to the signal region, and so this region is used to measure a two-dimensional template of dE/dx and η.

The contribution of any signal to the control regions is minimized by the inverted selection requirements. Only less than 10% of simulated signal events have either dE/dx or E_T^{miss} below the threshold values in the original signal region, while the backgrounds are significantly enhanced by inverting those requirements. The signal contamination is less than 1% in both control regions for all of the simulated masses and lifetimes considered in this analysis.

With those measured templates, the shape of the mass estimation is generated by first selecting a random (p, η) combination from CR1. This momentum value is combined with a dE/dx value taken from the appropriate distribution of dE/dx for the selected η from CR2. The use of η in both random samplings controls for any correlation between p, dE/dx, and η. Those values are then used to calculate a mass in the same way that is done for regular tracks in data, see Section 11.4.1. As this procedure includes all dE/dx values, the cut at 1.8 MeVg^{-1}cm^2 is then enforced to fully model the signal region. The generated mass distribution is then normalized by scaling the background estimate to the data in the region $M < 160$ GeV, where signals of this type have already been excluded [39]. This normalization takes place before the ionization requirement.

12.3 VALIDATION

The validity of the background estimation technique can be evaluated in both data and simulation. The underlying assumption that random combinations of dE/dx and momentum can predict a mass distribution in another region can be tested using simulated samples where concerns like multiple particle types can be controlled. Using the same technique in another set of signal-depleted regions in data then extends this confidence to the more complicated case where several particle species are inherently included.

12.3.1 CLOSURE IN SIMULATION

The first test of the procedure is done using a simulated sample of $W \to \mu\nu$ decays. These types of events provide the ingredients required to test the background estimate, E_T^{miss} and isolated tracks, with high statistics. In this example there is no signal, so simulated events in the orthogonal CRs are used to estimate the shape of the mass distribution of the simulated events in the signal region. To reflect the different topology for W boson decays, the CRs use slightly modified definitions. In all CRs, the requirement of $p > 150$ GeV and the SM rejection requirements are removed. Additionally, for the signal region the requirement on E_T^{miss} is relaxed to 30 GeV and the corresponding inverted requirement on CR2 is also set at 30 GeV.

With these modified selections, the simulated and randomly generated distributions of $M_{dE/dx}$ are shown in Figure 33. This figure includes the mass distributions before and after the requirement on dE/dx, which significantly shapes the distributions. In both cases the background estimation technique reproduces the shape of $M_{dE/dx}$ in the signal region. Their is a small difference in the positive tail of the mass distribution prior to the ionization cut, where the random events underestimate the fraction of tracks with mass above 150 GeV by about 20%. After the ionization requirement, however, this discrepancy is not present and the two distributions agree to within statistical uncertainties.

The ability of the technique to reproduce the shape in simulated events shows that the technique works as expected. No significant biases are acquired in using low dE/dx events to select kinematic templates or in using low E_T^{miss} events to

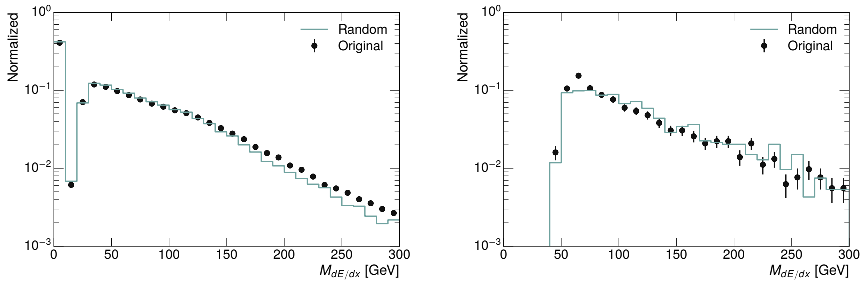

(a) (b)

Figure 33: The distribution of $M_{dE/dx}$ (a) before and (b) after the ionization requirement for tracks in simulated W boson decays and for the randomly generated background estimate.

select ionization templates, as either would result in a mismodeling of the shape of the mass distribution. The simulated events contain only one particle type, however, so this test only establishes that the technique works well when the the CRs are populated by exactly the same species.

12.3.2 VALIDATION REGION IN DATA

The second test of the background estimate is performed using data in an orthogonal validation region. The validation region, and the corresponding CRs, are formed using the same selection requirements as in the nominal method but with a modified requirement on momentum, $50 < p < 150$ GeV. This allows the technique to be checked in a region with very similar properties but that is signal depleted, as the majority of the signal has momentum above 150 GeV while the backgrounds are enhanced below that threshold. Any biases on the particle composition of the CRs will be reflected in the CRs used to estimate the mass distribution in the validation region.

13 SYSTEMATIC UNCERTAINTIES AND RESULTS

13.1 SYSTEMATIC UNCERTAINTIES

13.2 FINAL YIELDS

14 INTERPRETATION

14.1 CROSS SECTIONAL LIMITS

14.2 MASS LIMITS

14.3 CONTEXT FOR LONG-LIVED SEARCHES

PART VI

CONCLUSIONS

You can put some informational part preamble text here.

15 Summary and Outlook

15.1 Summary

15.2 Outlook

PART VII

APPENDIX

A INELASTIC CROSS SECTION

B

APPENDIX TEST

This appendix is temporary and is here to be used to check the style of the document.

Examples: *Italics*, Small Caps, ALL CAPS [1]. Acronym testing: **UML!** (**UML!**) – **UML!** – **UML!** (**UML!**) – **UML!s**

B.1 APPENDIX SECTION TEST

Random text that should take up a few lines. The purpose is to see how sections and subsections flow with some actual context. Without some body copy between each heading it can be difficult to tell if the weight of the fonts, styles, and sizes use work well together.

B.1.1 APPENDIX SUBECTION TEST

Random text that should take up a few lines. The purpose is to see how sections and subsections flow with some actual context. Without some body copy between each heading it can be difficult to tell if the weight of the fonts, styles, and sizes use work well together.

B.2 A TABLE AND LISTING

Curabitur tellus magna, porttitor a, commodo a, commodo in, tortor. Donec interdum. Praesent scelerisque. Maecenas posuere sodales odio. Vivamus metus lacus, varius quis, imperdiet quis, rhoncus a, turpis. Etiam ligula arcu, elementum a, venenatis quis, sollicitudin sed, metus. Donec nunc pede, tincidunt in, venenatis vitae, faucibus vel, nibh. Pellentesque wisi. Nullam malesuada. Morbi ut tellus ut pede tincidunt porta. Lorem ipsum dolor sit amet, consectetuer adipiscing elit. Etiam congue neque id dolor.

There is also a Python listing below Listing 1.

1 Footnote example.

LABITUR BONORUM PRI NO	QUE VISTA	HUMAN
fastidii ea ius	germano	demonstratea
suscipit instructior	titulo	personas
quaestio philosophia	facto	demonstrated

Table 3: Autem usu id.

B.3 SOME FORMULAS

Due to the statistical nature of ionisation energy loss, large fluctuations can occur in the amount of energy deposited by a particle traversing an absorber element[2]. Continuous processes such as multiple scattering and energy loss play a relevant role in the longitudinal and lateral development of electromagnetic and hadronic showers, and in the case of sampling calorimeters the measured resolution can be significantly affected by such fluctuations in their active layers. The description of ionisation fluctuations is characterised by the significance parameter κ, which is proportional to the ratio of mean energy loss to the maximum allowed energy transfer in a single collision with an atomic electron:

You might get unexpected results using math in chapter or section heads. Consider the `pdfspacing` option.

$$\kappa = \frac{\xi}{E_{\text{max}}} \tag{3}$$

E_{max} is the maximum transferable energy in a single collision with an atomic electron.

$$E_{\text{max}} = \frac{2m_e\beta^2\gamma^2}{1 + 2\gamma m_e/m_x + (m_e/m_x)^2},$$

where $\gamma = E/m_x$, E is energy and m_x the mass of the incident particle, $\beta^2 = 1 - 1/\gamma^2$ and m_e is the electron mass. ξ comes from the Rutherford scattering cross section and is defined as:

$$\xi = \frac{2\pi z^2 e^4 N_{Av} Z\rho\delta x}{m_e\beta^2c^2A} = 153.4\frac{z^2}{\beta^2}\frac{Z}{A}\rho\delta x \quad \text{keV},$$

where

z	charge of the incident particle
N_{Av}	Avogadro's number
Z	atomic number of the material
A	atomic weight of the material
ρ	density
δx	thickness of the material

κ measures the contribution of the collisions with energy transfer close to E_{max}. For a given absorber, κ tends towards large values if δx is large and/or if β is small. Likewise, κ tends towards zero if δx is small and/or if β approaches 1.

2 Examples taken from Walter Schmidt's great gallery: `http://home.vrweb.de/~was/mathfonts.html`

Listing 1: A floating example (`listings` manual)

```
for i in xrange(10):
    print i, i*i, i*i*i
print "done"
```

The value of κ distinguishes two regimes which occur in the description of ionisation fluctuations:

1. A large number of collisions involving the loss of all or most of the incident particle energy during the traversal of an absorber.

   As the total energy transfer is composed of a multitude of small energy losses, we can apply the central limit theorem and describe the fluctuations by a Gaussian distribution. This case is applicable to non-relativistic particles and is described by the inequality $\kappa > 10$ (i. e., when the mean energy loss in the absorber is greater than the maximum energy transfer in a single collision).

2. Particles traversing thin counters and incident electrons under any conditions.

   The relevant inequalities and distributions are $0.01 < \kappa < 10$, Vavilov distribution, and $\kappa < 0.01$, Landau distribution.

BIBLIOGRAPHY

[1] S. Agostinelli et al. “GEANT4: A simulation toolkit”. In: *Nucl. Instrum. Meth. A* 506 (2003), pp. 250–303. DOI: 10.1016/S0168-9002(03)01368-8.

[2] ATLAS Collaboration. “A study of the material in the ATLAS inner detector using secondary hadronic interactions”. In: *JINST* 7 (2012), P01013. DOI: 10.1088/1748-0221/7/01/P01013. arXiv: 1110.6191 [hep-ex]. PERF-2011-08.

[3] ATLAS Collaboration. “Electron and photon energy calibration with the ATLAS detector using LHC Run 1 data”. In: *Eur. Phys. J. C* 74 (2014), p. 3071. DOI: 10.1140/epjc/s10052-014-3071-4. arXiv: 1407.5063 [hep-ex]. PERF-2013-05.

[4] ATLAS Collaboration. “A measurement of the calorimeter response to single hadrons and determination of the jet energy scale uncertainty using LHC Run-1 pp-collision data with the ATLAS detector”. In: (2016). arXiv: 1607.08842 [hep-ex]. PERF-2015-05.

[5] ATLAS Collaboration. “Single hadron response measurement and calorimeter jet energy scale uncertainty with the ATLAS detector at the LHC”. In: *Eur. Phys. J. C* 73 (2013), p. 2305. DOI: 10.1140/epjc/s10052-013-2305-1. arXiv: 1203.1302 [hep-ex]. PERF-2011-05.

[6] ATLAS Collaboration. “The ATLAS Simulation Infrastructure”. In: *Eur. Phys. J. C* 70 (2010), p. 823. DOI: 10.1140/epjc/s10052-010-1429-9. arXiv: 1005.4568 [hep-ex]. SOFT-2010-01.

[7] T. Sjöstrand, S. Mrenna, and P. Skands. “A Brief Introduction to PYTHIA 8.1”. In: *Comput. Phys. Commun.* 178 (2008), pp. 852–867. DOI: 10.1016/j.cpc.2008.01.036. arXiv: 0710.3820.

[8] ATLAS Collaboration. *Summary of ATLAS Pythia 8 tunes*. ATL-PHYS-PUB-2012-003. 2012. URL: http://cds.cern.ch/record/1474107.

[9] A.D. Martin, W.J. Stirling, R.S. Thorne, and G. Watt. “Parton distributions for the LHC”. In: *Eur. Phys. J. C* 63 (2009). Figures from the MSTW Website, pp. 189–285. DOI: 10.1140/epjc/s10052-009-1072-5. arXiv: 0901.0002.

[10] A. Sherstnev and R.S. Thorne. “Parton Distributions for LO Generators”. In: *Eur. Phys. J. C* 55 (2008), pp. 553–575. DOI: 10.1140/epjc/s10052-008-0610-x. arXiv: 0711.2473.

[11] A. Ribon et al. *Status of Geant4 hadronic physics for the simulation of LHC experiments at the start of LHC physics program*. CERN-LCGAPP-2010-02. 2010. URL: http://lcgapp.cern.ch/project/docs/noteStatusHadronic2010.pdf.

[12] M. P. Guthrie, R. G. Alsmiller, and H. W. Bertini. “Calculation of the capture of negative pions in light elements and comparison with experiments pertaining to cancer radiotherapy”. In: *Nucl. Instrum. Meth.* 66 (1968), pp. 29–36. DOI: 10.1016/0029-554X(68)90054-2.

[13] H. W. Bertini and P. Guthrie. “News item results from medium-energy intranuclear-cascade calculation”. In: *Nucl. Instr. and Meth. A* 169 (1971), p. 670. DOI: 10.1016/0375-9474(71)90710-X.

[14] V.A. Karmanov. “Light Front Wave Function of Relativistic Composite System in Explicitly Solvable Model”. In: *Nucl. Phys. B* 166 (1980), p. 378. DOI: 10.1016/0550-3213(80)90204-7.

[15] H. S. Fesefeldt. *GHEISHA program*. Pitha-85-02, Aachen. 1985.

[16] G. Folger and J.P. Wellisch. “String parton models in Geant4”. In: (2003). arXiv: nucl-th/0306007.

[17] N. S. Amelin et al. “Transverse flow and collectivity in ultrarelativistic heavy-ion collisions”. In: *Phys. Rev. Lett.* 67 (1991), p. 1523. DOI: 10.1103/PhysRevLett.67.1523.

[18] N. S. Amelin et al. “Collectivity in ultrarelativistic heavy ion collisions”. In: *Nucl. Phys. A* 544 (1992), p. 463. DOI: 10.1016/0375-9474(92)90598-E.

[19] L. V. Bravina et al. “Fluid dynamics and Quark Gluon string model - What we can expect for Au+Au collisions at 11.6 AGeV/c”. In: *Nucl. Phys. A* 566 (1994), p. 461. DOI: 10.1016/0375-9474(94)90669-6.

[20] L. V. Bravin et al. “Scaling violation of transverse flow in heavy ion collisions at AGS energies”. In: *Phys. Lett. B* 344 (1995), p. 49. DOI: 10.1016/0370-2693(94)01560-Y.

[21] B. Andersson et al. “A model for low-pT hadronic reactions with generalizations to hadron-nucleus and nucleus-nucleus collisions”. In: *Nucl. Phys. B* 281 (1987), p. 289. DOI: 10.1016/0550-3213(87)90257-4.

[22] B. Andersson, A. Tai, and B.-H. Sa. “Final state interactions in the (nuclear) FRITIOF string interaction scenario”. In: *Z. Phys. C* 70 (1996), pp. 499–506. DOI: 10.1007/s002880050127.

[23] B. Nilsson-Almqvist and E. Stenlund. “Interactions Between Hadrons and Nuclei: The Lund Monte Carlo, Fritiof Version 1.6”. In: *Comput. Phys. Commun.* 43 (1987), p. 387. DOI: 10.1016/0010-4655(87)90056-7.

[24] B. Ganhuyag and V. Uzhinsky. “Modified FRITIOF code: Negative charged particle production in high energy nucleus nucleus interactions”. In: *Czech. J. Phys.* 47 (1997), pp. 913–918. DOI: 10.1023/A:1021296114786.

[25] ATLAS Collaboration. “Topological cell clustering in the ATLAS calorimeters and its performance in LHC Run 1”. In: (2016). arXiv: 1603.02934 [hep-ex].

[26] Peter Speckmayer. “Energy Measurement of Hadrons with the CERN ATLAS Calorimeter”. Presented on 18 Jun 2008. PhD thesis. Vienna: Vienna, Tech. U., 2008. URL: http://cds.cern.ch/record/1112036.

[27] CMS Collaboration. "The CMS barrel calorimeter response to particle beams from 2 to 350 GeV/c". In: *Eur. Phys. J. C* 60.3 (2009). DOI: 10.1140/epjc/s10052-009-0959-5.

[28] J. Beringer et al. (Particle Data Group). "Review of Particle Physics". In: *Chin. Phys. C* 38 (2014), p. 090001. URL: http://pdg.lbl.gov.

[29] P. Adragna et al. "Measurement of Pion and Proton Response and Longitudinal Shower Profiles up to 20 Nuclear Interaction Lengths with the ATLAS Tile Calorimeter". In: *Nucl. Instrum. Meth. A* 615 (2010), pp. 158–181. DOI: 10.1016/j.nima.2010.01.037.

[30] ATLAS Collaboration. "Jet energy measurement and its systematic uncertainty in proton–proton collisions at $\sqrt{s}$ = 7 TeV with the ATLAS detector". In: *Eur. Phys. J. C* 75 (2015), p. 17. DOI: 10.1140/epjc/s10052-014-3190-y. arXiv: 1406.0076 [hep-ex]. PERF-2012-01.

[31] Hung-Liang Lai, Marco Guzzi, Joey Huston, Zhao Li, Pavel M. Nadolsky, et al. "New parton distributions for collider physics". In: *Phys. Rev. D* 82 (2010), p. 074024. DOI: 10.1103/PhysRevD.82.074024. arXiv: 1007.2241 [hep-ph].

[32] E. Abat et al. "Study of energy response and resolution of the ATLAS barrel calorimeter to hadrons of energies from 20 to 350 GeV". In: *Nucl. Instrum. Meth. A* 621.1-3 (2010), pp. 134 –150. DOI: http://dx.doi.org/10.1016/j.nima.2010.04.054.

[33] ATLAS Collaboration. "Jet energy measurement with the ATLAS detector in proton–proton collisions at $\sqrt{s}$ = 7 TeV". In: *Eur. Phys. J. C* 73 (2013), p. 2304. DOI: 10.1140/epjc/s10052-013-2304-2. arXiv: 1112.6426 [hep-ex]. PERF-2011-03.

[34] ATLAS Collaboration. "Search for heavy long-lived charged R-hadrons with the ATLAS detector in 3.2 fb^{-1} of proton–proton collision data at $\sqrt{s}$ = 13 TeV". In: *Phys. Lett.* B760 (2016), pp. 647–665. DOI: 10.1016/j.physletb.2016.07.042. arXiv: 1606.05129 [hep-ex].

[35] A. C. Kraan, J. B. Hansen, and P. Nevski. "Discovery potential of R-hadrons with the ATLAS detector". In: *Eur. Phys. J.* C49 (2007), pp. 623–640. DOI: 10.1140/epjc/s10052-006-0162-x. arXiv: hep-ex/0511014 [hep-ex].

[36] K. A. Olive et al. "Review of Particle Physics". In: *Chin. Phys.* C38 (2014), p. 090001. DOI: 10.1088/1674-1137/38/9/090001.

[37] "dE/dx measurement in the ATLAS Pixel Detector and its use for particle identification". In: (2011).

[38] ATLAS Collaboration. "The ATLAS Simulation Infrastructure". In: *Eur. Phys. J.* C70 (2010), pp. 823–874. DOI: 10.1140/epjc/s10052-010-1429-9. arXiv: 1005.4568 [physics.ins-det].

[39] ATLAS Collaboration. “Search for metastable heavy charged particles with large ionisation energy loss in pp collisions at $\sqrt{s} = 8$ TeV using the ATLAS experiment”. In: *Eur. Phys. J. C* 75 (2015), p. 407. DOI: 10.1140/epjc/s10052-015-3609-0. arXiv: 1506.05332 [hep-ex]. SUSY-2014-09.

DECLARATION

Put your declaration here.

Berkeley, CA, September 2016

Bradley Axen

COLOPHON

Not sure that this is necessary.